catalysts

MDPI

Review

Recent Advances in Raman Spectroscopy for Resolving Material Surfaces/Interfaces

Tianyu Wang, Yingnan Jiang, Hongyu Feng, Linlin Liu *, Qingsong Deng, Danmin Liu and Cong Wang *

Beijing Key Laboratory of Microstructure and Property of Solids, College of Materials Science and Engineering, Beijing University of Technology, Beijing 100124, China; wtyuu@emails.bjut.edu.cn (T.W.); qsdeng@bjut.edu.cn (Q.D.)

* Correspondence: liulinlin@bjut.edu.cn (L.L.); smartswang@bjut.edu.cn (C.W.)

Abstract

Raman spectroscopy has become a key tool for resolving the molecular behavior of interfaces due to its non-invasiveness, fingerprinting ability and in situ detection advantages. Surface-enhanced Raman scattering (SERS) and its derivative techniques (including SHINERS and TERS) have significantly overcome the challenges of weak interfacial signals and strong water interference through the synergistic effect of electromagnetic field enhancement and chemical enhancement. They have realized highly sensitive molecular detection at various interfaces such as solid–liquid, gas–liquid, water–oil, and so on. Despite the challenges of substrate stability and signal quantization, the deep integration of multi-technology coupling and theoretical computation will further promote the breakthrough of this technology in interface science. In this review, we systematically review the applications of Raman spectroscopy and SERS techniques in interface resolution, including key research directions such as analyzing interfacial molecular structures, detecting material reactions at water–oil interface, and tracking the evolution of electrochemical interfacial species, as well as exploring the technological bottlenecks and future development directions.

Keywords: raman spectroscopy; surface-enhanced raman scattering (SERS); interface; catalysis; water splitting; multivariate curve resolution

check for updates

Academic Editor: Maurizio Muniz-Miranda

Received: 11 September 2025
Revised: 18 November 2025
Accepted: 21 November 2025
Published: 3 December 2025

Citation: Wang, T.; Jiang, Y.; Feng, H.; Liu, L.; Deng, Q.; Liu, D.; Wang, C. Recent Advances in Raman Spectroscopy for Resolving Material Surfaces/Interfaces. *Catalysts* **2025**, *15*, 1131. https://doi.org/10.3390/catal15121131

Copyright: © 2025 by the authors. Licensee MDPI, Basel, Switzerland. This article is an open access article distributed under the terms and conditions of the Creative Commons Attribution (CC BY) license (https://creativecommons.org/licenses/by/4.0/).

1. Introduction

Interfaces, the nanoscale boundaries where phases like solid, liquid, and gas meet, are central to myriad chemical and physical processes, including electrocatalysis, biomolecular recognition, and environmental remediation. As the bridge between a material's intrinsic properties and the external environment, surfaces and interfaces often define material performance. Unlike the bulk phase, surfaces possess unique structural and electronic properties due to unsaturated coordination sites, leading to stronger molecular interactions and enhanced chemical reactivity. Furthermore, the interfacial region is a complex and dynamic environment, comprising reactants, products, solvents, and electrolytes. Within it, key processes such as molecular adsorption, electron transfer, and surface reconstruction occur with high spatiotemporal complexity [1–4]. Consequently, molecular behavior at interfaces is dynamic, localized, and intricate. Probing critical aspects such as molecular orientation, hydrogen-bonding networks, and transient reaction intermediates remains a major challenge, underscoring the urgent need for advanced characterization techniques that can provide molecular-level insights to unravel these complex processes and establish clear structure–activity relationships.

In recent years, the rapid advancement of characterization techniques with nanoscale to atomic resolution has greatly deepened the understanding of structure–activity relationships at materials interfaces. The electron microscopy (Scanning Electron Microscopy SEM, Transmission Electron Microscopy TEM) and scanning probe methods (Atomic Force Microscopy AFM, Scanning Tunneling Microscopy STM) offer high-resolution morphological imaging [5–8], and X-ray-based methods (X-Ray Diffraction XRD, X-ray Absorption Spectroscopy XAS, X-ray Photoelectron Spectroscopy XPS) provide insights into crystallinity and elemental composition [9–11]. However, these techniques often face limitations in capturing dynamic molecular behavior and chemical identity under realistic or operando conditions, particularly for buried interfaces, liquid environments, or weakly adsorbed species.

Vibrational spectroscopies, including infrared spectroscopy and Raman spectroscopy, have thus become indispensable for retrieving chemical fingerprint information of interfacial molecules and reflecting the essence of physical processes within materials [12]. Among them, Raman spectroscopy stands out due to its broad spectral range, capability to probe low-frequency modes (e.g., lattice vibrations and intermolecular interactions), minimal interference from water, and applicability across gas, liquid, and solid phases without labeling [13–15]. Nevertheless, its utility in interfacial studies is inherently limited by the extremely low scattering cross-section and the sub-monolayer quantity of molecules present, making signal acquisition challenging with conventional Raman setups [16,17].

The emergence of surface-enhanced Raman scattering (SERS) has transformed this landscape by amplifying Raman signals by factors of 10^4–10^{10} via localized surface plasmon resonance on nanostructured metals [18,19]. This enhancement, driven by electromagnetic and chemical mechanisms, allows SERS to reach single-molecule sensitivity and perform in situ monitoring of interfacial processes while effectively quenching fluorescence background [20–22]. To overcome material and morphology constraints of traditional SERS substrates, techniques such as tip-enhanced Raman spectroscopy (TERS) and shell-isolated nanoparticle-enhanced Raman spectroscopy (SHINERS) have been developed [23–25]. These approaches extend Raman spectroscopy to a wider range of interfaces, enabling real-time tracking of molecular adsorption, orientation, hydrogen bonding, and reaction intermediates with high spatial and chemical specificity. By resolving molecular-level phenomena inaccessible to many other methods, SERS and its variants provide critical insights for the rational design and manipulation of functional interfaces.

Here, we review the progress of Raman spectroscopy and SERS techniques in the molecular scale analysis of different interfaces. In this review, we first briefly introduce the development and physical basis of Raman spectroscopy and SERS. We focus on the role of this technique in recent years in analyzing the molecular structures and roles of interfaces, investigating the physicochemical reactions (such as molecular adsorption/desorption, mass transfer, charge transfer) at water–oil interfaces, the dynamic evolution behavior of the surfaces/interfaces materials (including interfacial water, reaction intermediates and active sites) during electrocatalytic reactions, and exploring the reaction mechanisms. In addition, the integration of Raman spectroscopy with data processing for surface and interface studies are discussed. Finally, the challenges and prospects of Raman spectroscopy and SERS technology in the field of interfacial resolution are discussed.

2. Development and Foundations of Raman Spectroscopy

2.1. Development and Principles of Raman Spectroscopy

C.V. Raman first discovered the Raman scattering effect in 1928, and the spectroscopic technique based on this effect, known as Raman spectroscopy, has become a key spectroscopic tool in a variety of analytical fields [26]. In materials science, it is particularly valuable

because of its non-destructive, fast and informative nature. Raman spectroscopy provides the vibrational spectra of intramolecular bonds as a unique fingerprint for characterizing analytes.

Raman spectroscopy operates on the principle of inelastic light scattering. When monochromatic light interacts with a molecule, most photons are elastically scattered (Rayleigh scattering) without energy change. A tiny fraction, however, undergoes inelastic scattering, exchanging energy with the molecular vibrations and rotations. This results in a shift in the photon's frequency, known as Raman scattering, which comprises Stokes scattering and anti-Stokes scattering (Figure 1a). The energy difference between the incident and scattered photon, termed the Raman shift, corresponds directly to the vibrational energy levels of the molecular bonds [18]. This provides a unique "fingerprint" spectrum that allows for the identification of chemical structures, functional groups, and molecular isomers. The technique is universally applicable to gases, liquids, and solids, requiring minimal sample preparation.

Despite its strengths, conventional Raman spectroscopy is inherently limited by an extremely small scattering cross-section, leading to weak signals and low sensitivity. This fundamental constraint severely restricted its application for analyzing trace amounts of material or monolayer species at interfaces, until the advent of surface-enhanced Raman spectroscopy (SERS) dramatically overcame this barrier.

2.2. Fundamentals of SERS

Surface-enhanced Raman spectroscopy achieves remarkable signal amplification, with enhancement factors typically ranging from 10^4 to 10^{10}, by utilizing nanostructured materials primarily gold, silver, and copper [27,28]. This extraordinary sensitivity even permits the detection and characterization of single molecules. The underlying enhancement mechanisms are broadly classified into electromagnetic enhancement mechanism (EM) and chemical enhancement mechanism (CM), which often operate synergistically.

The electromagnetic mechanism is the dominant contributor to SERS intensity. It arises from the excitation of localized surface plasmon resonance (LSPR) in metallic nanostructures (Figure 1b). When incident light resonates with the collective oscillation of conduction electrons, it generates intensely localized electromagnetic fields, particularly at nanoscale gaps or sharp tips known as "hot spots". The Raman scattering intensity is proportional to the fourth power of this local field enhancement, which decays exponentially with distance from the metal surface [29,30].

Although the electromagnetic enhancement mechanism plays an important role in understanding SERS, there are still many experimental phenomena that cannot be explained by it. Complementing the EM, the chemical enhancement mechanism involves a charge-transfer process between the analyte molecule and the metal substrate [31,32]. Unlike the long-range EM effect, CM requires direct chemical adsorption (physisorption or chemisorption) of the molecule onto the surface. This interaction facilitates charge transfer, leading to the formation of a transient charge-transfer complex. The process effectively creates a new excited state, which can resonate with the incident light, thereby altering the molecular polarizability and significantly increasing the Raman scattering cross-section [33,34]. Figure 1c shows the schematic diagram of the charge transfer process. The CM is particularly significant for molecules that form strong chemical bonds with the metal surface and helps explain SERS phenomena that cannot be accounted for by EM alone. Although the contribution of CM to SERS enhancement is usually considered to be smaller than that of EM, the magnitude of the enhancement effect can still be up to 10^3 [35].

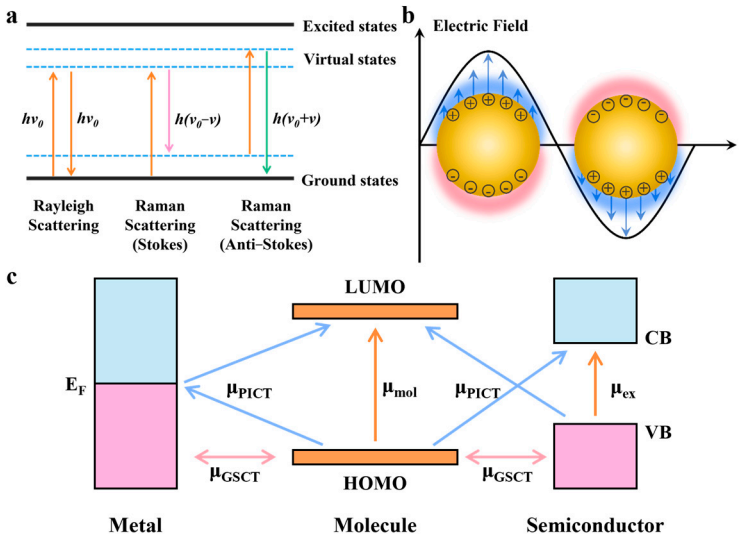

Figure 1. Fundamentals of SERS. (**a**) Raman Scattering and Rayleigh Scattering Schematics. (**b**) Schematic representation of LSPR of metal nanoparticles. (**c**) Chemical enhancement of SERS caused by electron transfer between base and molecule [31].

In most practical SERS applications, both electromagnetic and chemical enhancement effects coexist and synergize, enabling the ultra-sensitive, fingerprint-specific detection that makes SERS a powerful tool for interfacial analysis. Furthermore, the plasmonic enhancement in SERS can effectively quench fluorescence, thereby suppressing a major source of background interference in conventional Raman spectroscopy and significantly improving the signal-to-noise ratio for a wider range of analytes.

2.3. Expansion of SERS Technology

According to the electromagnetic mechanism, the SERS effect mainly comes from the excitation of surface plasmon resonances in free-electron metals with subwavelength structures. However, only a few metals such as Ag, Au and Cu, and some alkali metals can provide the significant enhancement required for strong Raman signal amplification. The practical applications involving other materials are severely limited, further limiting the versatility of SERS in various scientific and industrial environments [36]. In addition, these metals also require a specific surface morphology to achieve the significant enhancement properties of SERS. It has to be a metallic colloid with a surface with a certain roughness, island-like structure, or in the submicron size range. Therefore, SERS cannot be effectively applied to some structurally well-defined surfaces, further limiting its application [37].

SERS substrate with excellent performance is the core of SERS technology, and the fabrication of perfect SERS substrate with high sensitivity and high hotspot density is highly challenging [38]. Therefore, it is crucial to discuss the appropriate strategy to develop SERS active substrates.

In 1983, Van Duyne et al. proposed a "borrowed SERS activity" strategy to extend SERS to non-SERS active substrates [39]. They deposited discontinuous Ag islands on a non-SERS active substrate (semiconductor n-GaAs), and the molecules to be measured were pre-adsorbed on the semiconductor surface. The Raman scattering signals of adsorbed species on the semiconductor surface near the Ag islands were enhanced by utilizing the long-range effect of the strong electromagnetic field generated by the Ag islands with high SERS activity. The SERS signals of molecules adsorbed on the n-GaAs surface were successfully obtained. However, the SERS signals generated by molecules adsorbed on the Ag island would far exceed those adsorbed on the semiconductor, resulting in the elimination of the SERS signals of transition metal complex molecules adsorbed on the n-GaAs electrode.

In most cases, the molecules tend to diffuse through the surface and end up adsorbed on highly SERS-active materials that produce stronger signals. These signals mask the smaller signals from the non-SERS active surface of interest, thus complicating the analysis and reducing the effectiveness of the "borrowing" strategy [37]. In 1987, Fleischmann and Weaver et al. deposited an ultrathin layer of weak or non-SERS-active material on rough Ag and Au substrates [40,41]. Even if the target molecules were not in direct contact with the SERS-active substrate, the Raman signals of the target molecules near the surface could be enhanced by borrowing the strong electromagnetic field generated by the internal Ag or Au nanostructures. The "borrowed SERS activity" strategy has been continuously developed as further research, and the invention of tip-enhanced Raman spectroscopy (TERS) has realized a milestone breakthrough in the "borrowing" strategy. Shell-isolated nanoparticle-enhanced Raman spectroscopy (SHINERS) has further improved the strategy.

In 2010, Tian et al. developed SHINERS to address the limitations of SERS for single-crystal surfaces and the study of SERS inactive materials [23]. As a specific type of advanced SERS substrate, it employs Au nanoparticles coated with an ultrathin, pinhole-free, and chemically inert shell (e.g., silica, Al_2O_3), forming so-called shell-isolated nanoparticles (SHINs). A monolayer of these SHINs is dispersed onto the sample surface for detection. In this configuration, the Au core generates a powerful electromagnetic field that penetrates the thin shell, enhancing the Raman signals of molecules on the underlying substrate or at the shell–environment interface. The shell plays a critical dual role: it prevents direct contact between the plasmonic core and the sample (avoiding interference and protecting both), and it significantly improves the nanoparticle's stability under harsh conditions [42–44].

Parallel to the development of isolated nanoparticle strategies, the "Nanoparticle on Mirror" (NPoM) nanostructure has emerged as a powerful platform for generating intense and reproducible electromagnetic hotspots. In a typical NPoM configuration, a metal nanoparticle is precisely positioned atop a flat, extended metal film (the "mirror"), separated by a nanoscale gap [45]. This structure efficiently traps light within the sub-nanometer gap cavity, leading to enormous field enhancement. The gap size and the properties of the nanoparticles can be meticulously controlled, allowing for tailored plasmonic resonances and highly reproducible SERS signals [46,47]. This design not only achieves exceptionally high enhancement factors but also provides a well-defined and model-like system for fundamental studies of plasmonic coupling and light-matter interactions at the nanoscale.

Unlike SHINERS, which aims to modify the entire substrate, Tip-Enhanced Raman Spectroscopy (TERS) represents a distinctly different technical approach, achieving spatial resolution and signal enhancement through sophisticated instrumentation [48]. In 1985, the idea of TERS was first demonstrated by Wessel et al. [49] In 2000, Zenobi and Kawata et al. [50,51] realized the first TERS experiments, respectively, to further refine the theory of tip-enhanced Raman spectroscopy and to prove the feasibility of TERS [52]. TERS combines Raman spectroscopy with Scanning Probe Microscopy (SPM). When the Au or Ag tip acting as a Raman signal amplifier is very close to the surface of the molecule or material to be tested (less than 0.5 nm), under the excitation of a laser of a suitable wavelength, the electromagnetic field effect generated on the surface of the Au or Ag tip significantly enhances the Raman signals of the molecule to be tested in the vicinity of the tip. This technique not only allows the extension of the surface for SERS studies to smooth surfaces with atomic-level flatness, but also enables spatial resolution on the order of a few nanometers.

In principle, TERS is expected to solve the problem of substrate and surface universality, since the Raman signal from any substrate, regardless of the material and surface smoothness, can be increased by borrowing tip-vertex enhancement. However, TERS strongly relies on complex instrumentation and its total Raman signal is very low because

the TERS technique provides only one hot spot at a given time. These problems make TERS somewhat limited in many applications [37].

In summary, the selection of an appropriate SERS-based method hinges on aligning the technique's inherent strengths with the analytical goals. Conventional SERS, employing colloids or nanostructured surfaces, delivers the highest enhancement factors, making it ideal for detecting ultra-trace analytes in solution or on compatible rough surfaces, albeit with limited versatility on arbitrary, smooth substrates. For investigations demanding the highest spatial resolution, TERS is unparalleled, though its operational complexity and slower signal acquisition present practical trade-offs. Bridging these extremes, SHINERS offers a robust compromise by transforming virtually any surface whether conductive, insulating, single-crystalline, rough, or smooth into an active SERS substrate. While its sensitivity is lower than that of direct-contact SERS, SHINERS provides a reproducible and widely applicable platform for in situ interfacial analysis, particularly where direct contact with a plasmonic metal is undesirable.

3. Application of Raman Spectroscopy in Interface Resolution

3.1. Studying the Molecular Structure and Roles of Interfaces

3.1.1. Solid–Liquid Interface

The solid–liquid interface is a critical region where processes like adsorption, catalysis, and (bio)chemical reactions occur. Understanding the molecular structure and dynamics at these interfaces is fundamental in fields like environmental science. SERS has emerged as a powerful tool not only for the ultrasensitive detection of aquatic pollutants but also for probing their specific interactions with solid substrates at the interface. By concentrating target molecules within the electromagnetic "hot spots" at the nanostructured solid surface, SERS provides a unique window into the adsorption behavior, orientation, and transformation of molecules at the solid–liquid interface.

A primary strength of SERS is its ability to reveal not just the identity but also the orientation, conformation, and local environment of molecules at the interface. This is exemplified by studies on ionic liquid–electrode interfaces. Niu et al. [53] utilized SERS to investigate the potential-dependent adsorption behavior of water and ionic liquids on a Ag electrode surface in ionic liquids containing different concentrations of water. By analyzing changes in the vibration frequency of the OH stretching mode, they derived the configuration of water at the ionic liquid/electrode interface and the relationship between the zero-charge potential (pzc) and the molar fraction of water. In solutions with lower water content, water molecules exist in the interface layer through hydrogen bonding with cations. In solutions with higher water content, intermolecular hydrogen bonding between water molecules is strengthened, increasing the likelihood of direct interaction between water molecules and the electrode surface. Similarly, Chen et al. [54] used SERS to study the host-guest interactions between cucurbit[7]uril (CB[7]) and methyl violet ($MV^{2+}2I^{-}$) at the Au NP–water interface. The sensitivity and rich molecular vibrational information provided by SERS (Figure 2a) enabled the determination of cooperative adsorption between counter anions (I^{-} and Br^{-}), guest cations (MV^{2+} and Na^{+}), and hosts (CB[n], cucurbit[n]uril, n = 5, 6, 7) on the surface. Based on SERS results, a repulsive complex model between CB[7] and MV^{2+} was proposed, differing from that in aqueous solutions. This study provides new insights into the fundamental understanding of host-guest interactions at solid–liquid interfaces and holds promise for applications in the host-guest chemistry of engineered nanomaterials.

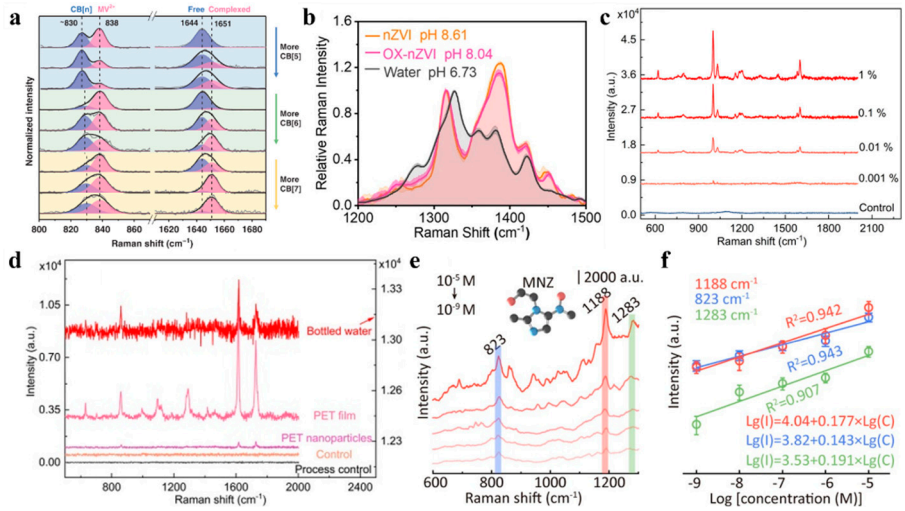

Figure 2. (**a**) CB[5]/CB[6]/CB[7] concentration-dependent SERS spectra obtained with 2.5 μM $MV^{2+}2I^{-}$ [54]. (**b**) Average Raman spectra of Interface-Py-Azo-pH adsorbed on nZVI and OX-nZVI in deionized water, with the standard deviations shown as shades above and below the spectra, respectively ($n \geq 3$) [55]. (**c**) Raman spectra of 50 nm PS nanoplastics with concentrations varying from 1 to 0.001% on TCA substrates and on a plain glass substrate at a concentration of 1% (control line). (**d**) Raman spectra of the sample extracted from bottled drinking water on the TCA substrate (red line), the plain glass substrate (brown line), and the PET film (purple line) [56]. (**e**) Raman spectra of MNZ with different concentrations (10^{-5} M–10^{-9} M) in situ collected by superhydrophobic ZnO/Ag NWs. (**f**) Linearity between peak intensity and MNZ concentration [57].

Beyond static structure, SERS can function as a real-time probe for dynamic processes at the interface, including chemical reactions and mass transfer. Ma et al. [55] demonstrated an azo-enhanced Raman scattering strategy, designed a 2 nm-long small-molecule pH probe anchored to a solid surface via chelating groups. By leveraging intramolecular Raman enhancement sensitivity, the probe directly observed proton transfer between water and nanozero-valent iron (nZVI, a well-known environmental material for pollution control) (Figure 2b). The study found that the interface acidity increased after oxalate modification of nZVI, confirmed the subsequent efficiency of advanced phosphate adsorption, and elucidated the potential mechanism of proton transfer from water to nZVI driven by ion exchange compared to unmodified nZVI. This capability to monitor dynamics extends to flowing systems. Dou et al. [58] developed a robust SERS substrate for the real-time monitoring of malachite green in flowing water, showcasing the potential to track adsorption and transport phenomena at solid–liquid interfaces under dynamic conditions.

The drive to study a wide range of interfacial interactions, from the adsorption of small antibiotic molecules to the weak adhesion of nanoplastics, has spurred continuous innovation in SERS substrate design. The core principle is to concentrate the target analytes at the substrate-solution interface and enhance their inherently weak Raman signals, thereby enabling both detection and interfacial behavior analysis. For nanoplastics, which present a challenge due to their weak Raman scattering, strategies focus on efficient interfacial enrichment and hotspot generation. Hu et al. [59] developed a quantitative SERS method for detecting polystyrene nanoplastics (50–500 nm) in water using silver nanoparticles and potassium iodide (KI). The KI served a dual function: it cleaned impurity ions from the Ag NP surfaces and induced their aggregation to form SERS "hot spots," thereby significantly enhancing the Raman signal of the nanoplastics. This approach achieved a low detection limit of 6.25 μg/mL for 100 nm nanoplastics and established a strong linear relationship ($R^2 > 0.970$) between SERS intensity and nanoplastic concentration, enabling reliable quantification. The method demonstrated practical utility with satisfactory recover-

ies (87.5–110%) in spiked lake water samples. Ruan et al. [60] established a SERS method for detecting nanoplastics in water using a silver nanoparticle sol system with NaI as an aggregating agent. This method enables semi-quantitative detection by correlating the SERS intensity at characteristic peaks (e.g., 1003 cm^{-1} for PS) with plastic concentration, based on calibration curves constructed using PS particles of known sizes (20 nm–5 μm) and concentrations (1–0.0005%). Key factors affecting signal enhancement, such as aggregating agent type, particle size, and measurement timing, were optimized experimentally. NaI was selected for its ability to promote "hot spot" formation between Ag NPs and plastics, while UV-vis and SEM were used to monitor aggregation states. The method achieved a notable detection limit of 0.0005%, and was successfully applied to real samples such as mineral water and expanded polystyrene packaging leachate, where nanoplastic concentrations were quantified at the μg/L level.

Another strategy involves utilizing engineered solid substrates with well-defined nanostructures. Zhang et al. [56] employed a lithographically fabricated gold triangular cavity array (TCA) as a highly sensitive SERS substrate. This platform enabled the detection of 50 nm polystyrene nanoplastics down to a concentration of 0.001% and successfully identified PET nanoplastics of ~88.2 nm in commercially bottled water (Figure 2c,d). The corresponding Raman spectra and mapping images visually confirm the sensitive detection and spatial distribution of nanoplastics on the substrate, highlighting its capability for trace analysis and quantification in real-world samples. Carreón et al. [61] developed a SERS-based method using Ag–Au bimetallic nanoparticle films to detect nanoplastics, where Raman spectroscopy identifies specific vibrational fingerprints of PET, such as C=O stretching at 1724 cm^{-1}. The concentration of nanoplastics is quantified by establishing a linear calibration curve between the SERS peak intensity and the known concentrations of PET dispersions. Key factors like substrate uniformity and reproducible "hotspot" distribution were controlled to ensure reliable signal enhancement without using external aggregating agents. This approach enables sensitive and direct quantification of nanoplastic concentrations in complex samples based on characteristic Raman bands. The research group [62] developed a flexible SERS substrate using three-dimensional dendritic Au films for sensitive detection of nanoplastics. Raman spectroscopy identifies nanoplastics by their unique vibrational fingerprints, such as the C=O stretching peak at 1724 cm^{-1} for PET. The concentration is quantified using a linear calibration curve derived from the relationship between the SERS peak intensity and known nanoplastic concentrations. This approach allows for direct, label-free quantification of nanoplastic levels in complex samples without the need for aggregating agents or machine learning, leveraging the intrinsic Raman signal enhanced by the substrate's uniform hotspots. Xing et al. [63] developed a SERS method using a superhydrophobic AuNP substrate to detect and quantify trace nanoplastics in water. Quantification is achieved via a calibration curve, correlating SERS intensity of characteristic peaks (e.g., 1000 cm^{-1} for PS) with nanoplastic concentration, without using aggregating agents or machine learning. Factors like particle size and concentration affecting signal enhancement were systematically evaluated to define the model's applicable range. The method successfully identified PET nanoplastics in bottled water at trace levels (μg/L) and detected nanoplastics in river water after sample pre-concentration, demonstrating high sensitivity for real environmental monitoring.

For comprehensive analysis, Li et al. [64] developed an integrated SEM-Raman method to address the challenge of accurately identifying individual micro/nanoplastics (MNPs). This approach leverages Raman spectroscopy to provide a definitive "chemical fingerprint" that complements the morphological data obtained from SEM. To overcome the weak Raman signal of nanoplastics and the charging effects of insulating plastics under electron beams, gold nanoparticles (Au NPs) were introduced as a SERS substrate. Simply mixed

with the sample, the Au NPs adsorb onto plastic surfaces, serving a dual function: (1) acting as a conductive layer to enable clear SEM imaging, and (2) enhancing the Raman signal via localized surface plasmon resonance, enabling the detection of characteristic peaks from single PS and PMMA particles as small as 500 nm and 300 nm, respectively. By simultaneously resolving the key issues of signal enhancement and charge dissipation, this method enables concurrent morphological and chemical identification of MNPs at the single-particle level, advancing detection capabilities from the microscale to the sub-microscale. Li et al. [65] developed a sustainable method using an olive oil-in-water emulsion to efficiently separate and concentrate microplastics and nanoplastics from complex matrices like seawater and toothpaste via hydrophobic interactions. Following demulsification and enrichment, Raman spectroscopy was employed to successfully identify the specific polymer types, such as PS and PMMA, by their unique spectral fingerprints. This demonstrates Raman spectroscopy's critical role in providing definitive chemical identification at the interface between the enriched plastic particles and the complex sample matrix, enabling accurate analysis even after extraction.

For antibiotic molecules, substrate design often incorporates specific functionalities for enhanced interfacial capture. Shao et al. [66] developed a magnetic SERS platform using Au/Fe_3O_4/MIL-101(Cr) for trace antibiotic detection. Raman spectroscopy identifies sulfapyridine through its characteristic vibrational peaks, such as S–N and C–C stretches at 1001 cm^{-1} and 1587 cm^{-1}. Quantitative analysis is achieved by combining principal component analysis (PCA) to handle multi-peak signals and a linear calibration model correlating peak intensity with antibiotic concentration. This method enables sensitive, reproducible detection without aggregating agents, leveraging the MOF's enrichment capability and magnetic separation for practical sample analysis. Liu et al. [57] developed a superhydrophobic SERS platform based on ZnO/Ag nanowires for in situ monitoring of trace antibiotics in harsh aqueous environments. Raman spectroscopy enables sensitive identification of metronidazole (MNZ) through characteristic vibrational peaks such as C-H rocking at 823 cm^{-1} (Figure 2e). Quantitative analysis is achieved using a linear calibration model correlating SERS intensity with antibiotic concentration, as illustrated in Figure 2f, which shows a clear linear relationship across different MNZ levels. This hydrophobic substrate enhances both analyte enrichment and localized electric fields, allowing reliable detection down to 10^{-9} M without aggregating agents, even in flowing or corrosive water conditions.

For Per- and Polyfluoroalkyl Substances (PFAS), strategies similarly focus on efficient interfacial enrichment and hotspot generation. Feng et al. [67] constructed a highly sensitive SERS substrate featuring a plasmonic Ag nanoparticle/Au@Ag nanorod sandwich structure for the direct detection of PFAS. This design specifically probed the solid–liquid-air interface during the dynamic droplet evaporation process. As the solvent evaporated, the "nanopump effect" actively concentrated PFAS molecules into the electromagnetic hotspots within the nanogaps between the top AgNPs and the bottom Au@AgNR monolayer. This interfacial enrichment, combined with the strong electromagnetic coupling in the sandwich structure, enabled direct SERS identification and quantitative detection of various PFAS down to 0.1 ppm using a portable Raman spectrometer. Their work demonstrates how strategically engineered nanostructures can harness interfacial phenomena to concentrate analytes and amplify signals, enabling direct, on-site SERS analysis. Kukralova et al. [68] demonstrated how SERS transcends its role as a mere detection tool. Their study centered on a strategically engineered interface: a porous Au-silicon substrate functionalized with positively charged -NH_2 groups. While electrochemical impedance signaled a non-specific change at the electrode surface, SERS provided the critical molecular-level evidence that validated the interfacial process. The appearance of characteristic C–F vibrational bands (e.g.,

at 718 cm^{-1} for PFOA) in the SERS spectrum served as a direct "fingerprint," conclusively proving that the observed signal originated from the specific adsorption of PFAS molecules onto the functionalized surface. This work underscores SERS's unique capability not only to identify pollutants but also to verify the success and specificity of interfacial capture mechanisms, which is vital for developing reliable environmental sensors. Lada et al. [69] developed a generic SERS method for detecting PFAS by leveraging an ion-pairing mechanism. In their approach, PFAS molecules from the aqueous phase form ion pairs with the cationic dye methylene blue (MB), which are subsequently extracted into chloroform. Crucially, the interfacial transfer and enrichment efficiency of these PFAS-MB complexes were quantitatively linked to the original PFAS concentration. The final SERS detection was not performed in the organic phase but after a key interfacial dissociation step, where the MB was released back into an aqueous solution. This dissociation process, optimized for efficiency, allowed the liberated MB molecules to freely interact with the aqueous Ag colloidal SERS substrate. By quantifying the SERS signal of MB, the method indirectly determined the PFAS concentration with a remarkable detection limit down to 5 ppt. This work underscores how SERS can be coupled with designed interfacial chemistry (liquid–liquid extraction and dissociation) to overcome inherent detection limitations, transforming an indirect chemical process into a sensitive and generic analytical tool for pollutants at the nexus of different phases.

3.1.2. Gas–Liquid Interface

The gas–liquid interface represents a unique chemical environment where molecular organization, solvation, and local electric fields deviate dramatically from the bulk phase, governing processes from atmospheric chemistry to catalysis. Conventional bulk analytical techniques often fail to capture the distinct molecular behaviors at this boundary. Raman spectroscopy overcomes this limitation by providing in situ vibrational fingerprints of interfacial species, enabling direct probing of reaction pathways, molecular structure, and the influence of interfacial fields.

A key strength Raman spectroscopy lies in its ability to track reaction kinetics within individual microdroplets, functioning as confined reactors. The study by Mohajer et al. [70] exemplifies the application of Raman spectroscopy in probing unique reactivity at gas–liquid interfaces. By monitoring a single trapped micron-sized ammonia-containing droplet exposed to a CO_2 atmosphere, they observed the emergence and growth of a Raman band at ~1008 cm^{-1} (Figure 3a,b). Deconvolution of this band confirmed contributions from urea (~1003 cm^{-1}) and bicarbonate (~1013 cm^{-1}), providing direct evidence for the spontaneous formation of urea within the droplet's surface layer. Crucially, control experiments ruled out the involvement of NH_4^+ and identified unprotonated NH_3 as the essential precursor, highlighting the decisive role of the interfacial microenvironment. This demonstrates how interfacial gradients, such as in pH, can stabilize reactive intermediates like neutral carbamic acid and facilitate a proton-catalyzed pathway to urea. This reaction is suppressed in bulk solution. This work underscores the value of Raman spectroscopy in elucidating how surface and interfacial phenomena, including molecular organization and chemical potential gradients, can fundamentally alter reaction pathways and kinetics, offering critical insights for understanding and designing interfacial processes in materials science. Zhang et al. [71] leveraged confocal Raman spectroscopy as a primary tool to probe the molecular behavior and reaction kinetics at the gas–liquid interface during nitrate photolysis in microdroplets. In their study, a single microdroplet with a radius of 15 μm served as a confined reactor, and the interface-specific reaction was tracked in real-time by monitoring the evolution of Raman bands. They used the sulfate ion (SO_4^{2-}) peak at 980 cm^{-1} as an internal standard, normalizing the nitrate ion (NO_3^-) peak at 1050 cm^{-1}

to account for any signal fluctuations (Figure 3c). The temporal decay of the intensity ratio (A_{1050}/A_{980}) provided a direct spectroscopic measure of the nitrate loss rate, enabling the precise quantification of the photolysis rate coefficient (j). Complementary size-dependence studies, supported by aerosol optical tweezers, further confirmed that the reaction was surface-driven, as j scaled inversely with the droplet radius below a critical size. The Raman data thus provided direct evidence that the air–water interface is the dominant reaction site, highlighting the technique's power in elucidating how surface properties govern molecular processes and kinetics in confined systems.

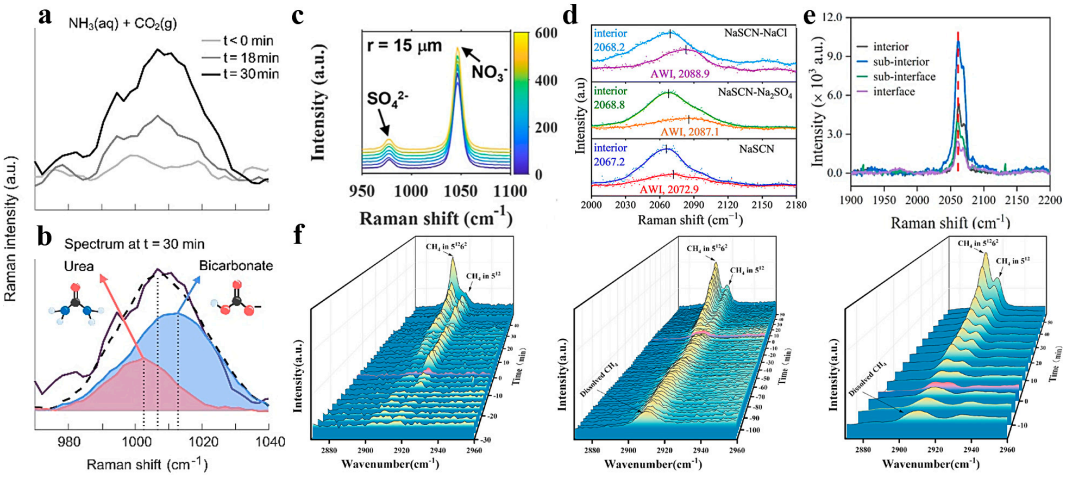

Figure 3. (**a**) Single-droplet Raman spectra recorded before (t < 0 min) and after (t > 0 min) exposure of an aqueous ammonia [NH_3(aq)] droplet (radius 2 μm) to CO_2 gas [CO_2(g)]. (**b**) The decomposition of the Raman spectrum at t = 30 min (full black line) shows that urea (red, 33 mM) was formed in addition to bicarbonate (blue, 83 mM). The dashed black line is the sum spectrum of urea and bicarbonate. The vertical dotted lines indicate the positions of the band maxima of urea (1003 cm^{-1}), the sum spectrum (1008 cm^{-1}), and the bicarbonate (1013 cm^{-1}) [70]. (**c**) Raman spectra of a 15 μm radius droplet during nitrate photolysis under 310 nm UV light at 70% RH. The color bar indicates the reaction time. Peaks at 980 cm^{-1} and 1050 cm^{-1} were attributed to SO_4^{2-} and NO_3^-, respectively [71]. (**d**) Raman spectra of ν(C≡N) in the interior and at the air–water interface of the microdroplet containing 2 M NaSCN and 0.2 M NaCl or 0.2 M Na_2SO_4. Microdroplet diameter, ~48 mm [72]. (**e**) SERS analysis of ν(C≡N) measured in different regions of microdroplets containing 1 M NaSCN and 1 g L^{-1} HULIS, with an average microdroplet diameter of ~30 μm [73]. (**f**) In situ Raman spectra of the system containing pure water, 0.5 wt% PMAM-b-PVL, and 0.5 wt% Luvicap EG, respectively. (The time corresponding to the purple Raman diagram represents the onset of hydrate formation, while the preceding period is referred to the induction time.) [74].

Beyond tracking reactants and products, Raman spectroscopy can quantitatively probe the interfacial environment itself, such as the intense electric fields that often govern reactivity. Li et al. [75] systematically elucidated the mechanism behind the significantly accelerated photochemical degradation of perfluorooctanoic acid (PFOA) at the air–water interface (AWI) of microdroplets using simulated Raman scattering (SRS) microscopy, vibrational Stark effect measurements, and density functional theory (DFT) calculations. Their work revealed that the dramatic rate enhancement stems from the synergistic effects of reactant concentration enrichment, an ultrahigh interfacial electric field (~6×10^7 V/cm), and partial solvation at the microdroplet interface, which collectively lower the energy barriers of key photocatalytic steps. Raman spectroscopy played a pivotal role by not only imaging the spatial enrichment of reactants at the interface but also quantitatively probing the interfacial electric field in situ via the vibrational Stark effect, unambiguously demonstrating the critical function of the unique microdroplet interfacial environment in

enhancing pollutant degradation. In a subsequent study [72], the same group achieved highly efficient photocatalytic H_2O_2 production within microdroplets and further investigated the underlying interfacial mechanisms. Using micro-Raman spectroscopy, they monitored the Raman shift of the cyano group stretch vibration, ν(C≡N), which is highly sensitive to external electric fields. The ν(C≡N) peak was observed to shift from approximately 2065.5 cm^{-1} in the droplet interior to 2070.4 cm^{-1} at the AWI in a 48 μm droplet containing 2 M NaSCN (Figure 3d), directly confirming the presence of a strong interfacial electric field. The addition of salts like Na_2SO_4 and NaCl further increased this Raman shift difference, corresponding to enhanced electric field strengths and demonstrating the role of the electric double layer in promoting photocatalytic H_2O_2 synthesis. Furthermore, by tracking the O-O stretching vibration of H_2O_2 in individual droplets via in situ Raman spectroscopy, the study confirmed that the photocatalytic H_2O_2 decomposition efficiency was higher at the AWI than in the interior, underscoring the role of the ultrahigh interfacial electric field and partial solvation in accelerating charge separation and interfacial reaction kinetics. The group [73] also employed a microdroplet-printing system combined with SERS, transient absorption spectroscopy, and DFT calculations to investigate the dramatically accelerated photosensitized formation of sulfate at the air–water interface (AWI) of humic-like substance (HULIS) microdroplets. Their study revealed a 3–4 orders of magnitude enhancement in sulfate production rates in aerosol- and cloud-relevant microdroplets compared to conventional bulk-phase reactions. Notably, SERS analysis of the cyanide stretch vibration, ν(C≡N), within HULIS-containing microdroplets showed negligible Stark shift (Figure 3e), ruling out a strong interfacial electric field as the primary accelerator, which is in stark contrast to previous microdroplet systems. DFT calculations further confirmed a lower electron transfer energy barrier at the interface (0.83 eV) compared to the bulk phase (1.14 eV), highlighting the role of interfacial solvent organization in promoting rapid sulfate formation. This work demonstrates how Raman-based interfacial analysis, combined with theoretical modeling, can disentangle complex surface-driven reaction mechanisms in atmospheric aerosol systems.

Furthermore, Raman spectroscopy is exceptionally capable of characterizing molecular organization and structure at the interface. Guo et al. [76] employed in situ SERS to probe the molecular structure of a dipalmitoylphosphatidylcholine (DPPC) Langmuir monolayer at the air–water interface. The Raman scattering spectra provided the most direct evidence for pressure-induced conformation ordering, capturing four distinct features in the C-H stretching vibration region (2800–3000 cm^{-1}) under four different surface pressures. Crucially, quantitative analysis of the intensity ratio between the ~2932 cm^{-1} and ~2848 cm^{-1} bands revealed this ratio as a sensitive indicator of alkyl chain conformation ordering. This ratio increases from 0.654 at 1 $mN{\cdot}m^{-1}$ to 0.873 at 45 $mN{\cdot}m^{-1}$, providing conclusive spectroscopic evidence for the transition of alkyl chains from disordered to ordered states during monolayer compression. This data directly links interfacial packing pressure to molecular-level structural changes, highlighting Raman spectroscopy's powerful capability in quantifying dynamic behavior at fluid interfaces. Wan et al. [74] employed in situ Raman spectroscopy to elucidate the molecular mechanism by which their biodegradable amphiphilic copolymer, PMAM-b-PVL, inhibits methane hydrate formation. The most direct and convincing evidence is presented in Figure 3f, which compares the Raman spectra during hydrate formation in a pure water system versus one containing the inhibitor. In the pure water system, the characteristic peaks for methane in small and large hydrate cages appear rapidly after nucleation. In stark contrast, the spectrum for the PMAM-b-PVL system during the induction period shows only a prominent peak for dissolved methane at 2910 cm^{-1}, with a significant delay in the appearance of the cage signals. Combined with other findings, this clearly reveals the dual mechanism of action for amphiphilic

polymers: they enrich methane at the interface via hydrophobic interactions while simultaneously disrupting the local water structure through their hydrophilic groups, thereby effectively impeding the formation of critical hydrate cages and modifying the hydrate crystal composition.

In summary, by bridging the gap between macroscopic observation and microscopic insight, Raman spectroscopy is vital for unraveling the complex molecular behaviors that define the gas–liquid boundary.

3.1.3. Solid–Solid Interface

Solid–solid interfaces define the properties of many advanced materials, yet their specific chemical and structural features are challenging to probe. Raman spectroscopy overcomes this by providing direct, in situ vibrational fingerprints of the interface. Its ability to map spatial distribution and identify molecular interactions from the micro- to nanoscale makes it indispensable for linking interfacial structure to material performance.

At both macro and micrometer scales, Raman imaging technology enables visualization of the compositional distribution and coverage state at interfaces. Arunagiri et al. [77] employed Raman spectroscopy and 3D Raman mapping to conduct an in-depth analysis of the surface and interface characteristics of the PCL/PDLLA-modified melamine sorbent, specifically evaluating the spatial distribution and coverage of the polymer coating on the melamine sponge skeleton. In their study, Raman spectroscopy (Figure 4a) was used to identify the characteristic vibrational peaks of both PCL/PDLLA and melamine within the composite material, notably the OCH vibration peak at 2942 cm^{-1} (representing PCL/PDLLA) and the triazine ring vibration peak at 976 cm^{-1} (representing the melamine sponge). The distribution of these components in three-dimensional space was further visualized via 3D Raman mapping (Figure 4b,c). The results demonstrated that the green signal intensity, corresponding to PCL/PDLLA, progressively increased along the Z-axis direction, while the yellow signal, representing the melamine's triazine ring, concurrently decreased. This trend was particularly evident from the 4th to the 10th layers of the stacked images (Figure 4c), clearly revealing the formation of a continuous and gradually thickening PCL/PDLLA coating on the melamine scaffold. This Raman mapping analysis not only confirmed the successful and uniform coating of PCL/PDLLA onto the macroporous structure of the melamine sponge but also elucidated the physical integration state at the interface between the polymer and the sponge matrix, providing crucial evidence related to surface structure for understanding the material's selective wettability and stability during the oil/water separation process. Qiang et al. [78] utilized Raman spectroscopy to investigate the structural changes in graphene oxide nanoribbons (GONRs) before and after surface functionalization with two different silane coupling agents, TMOS and FAS. The Raman spectra (Figure 4d) displayed characteristic D (~1335 cm^{-1}) and G (~1580 cm^{-1}) bands for all samples. A key finding was the increase in the ID/IG ratio from ~0.93 for pristine GONRs to ~1.13 for TMOS-f-GONR and ~1.11 for FAS-f-GONR. This increase indicates a higher degree of structural defects within the GONR sheets, which the authors attributed to the successful covalent bonding between the silane molecules and the GONR surface during the functionalization process. This Raman analysis, corroborated by FTIR and XPS results, confirmed the effective chemical modification, which was crucial for transforming the surface property of the final PU sponge composite from merely hydrophobic to super-hydrophobic, thereby enabling its efficient performance in oil/water separation under both static and dynamic states.

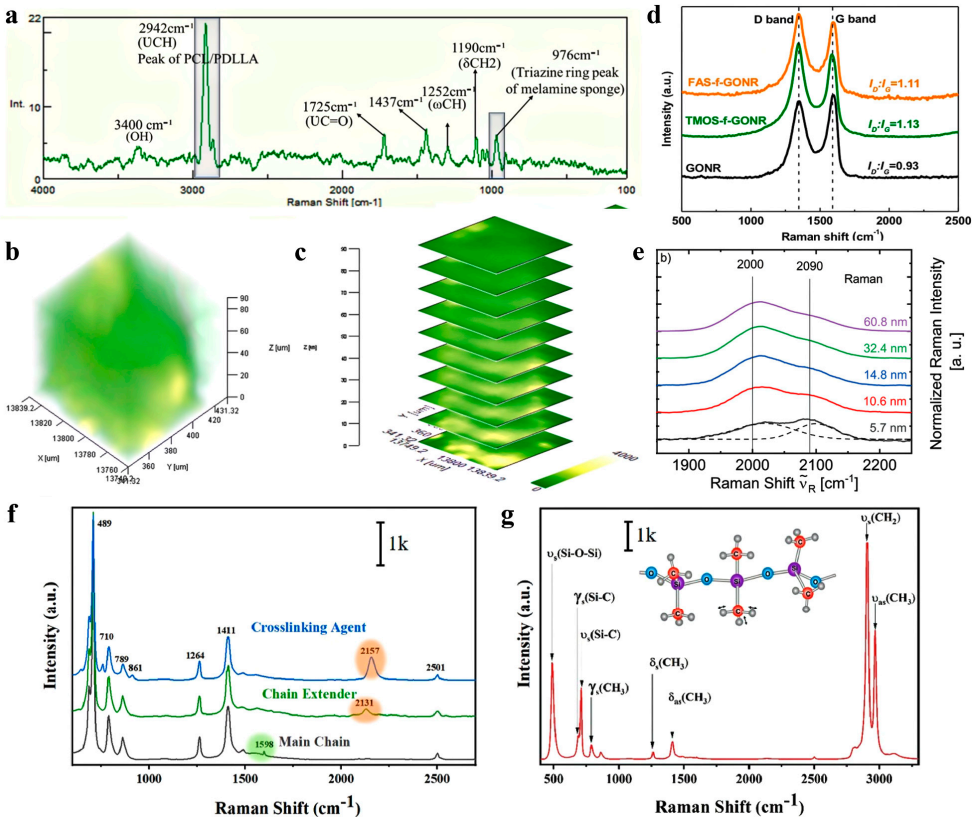

Figure 4. Raman mapping analysis of PCL/PDLLA (80:20) modified melamine sorbents (**a**) Raman peaks, (**b**) 3D Raman mapping, and (**c**) 3D stacking image [77]. (**d**) Raman spectra of GONR, TMOS-f-GONR and FAS-f-GONR, respectively [78]. (**e**) FTIR absorption spectra and corresponding Raman intensity spectra normalized by the layer thickness of intrinsic a-Si:H layers of various thicknesses deposited at P_P = 300 W versus the wavenumber $\tilde{\nu}_{IR}$ and the Raman shift $\tilde{\nu}_{IR}$, respectively. The sample thicknesses are indicated on the right side of the graphs. The dashed lines show the double Gaussian function fits for the film of 5.7 nm thickness [79]. (**f**) Raman spectroscopy of main components of the Al/PDMS composites. (**g**) Raman spectroscopy and molecular structure of Al/PDMS composites [80].

Dynamic evolution of interfaces during preparation or service, Fischer et al. [79] investigated the Si-H bond configuration at the amorphous silicon/crystalline silicon (a-Si:H/c-Si) interface in silicon heterojunction solar cells. The study confirmed that Raman spectroscopy can penetrate the ITO layer and is applicable to textured substrates, enabling the first in situ monitoring of microstructural parameters of the a-Si:H layer within the finished cell (Figure 4e), providing critical technical support for optimizing the interface passivation mechanism. Luo et al. [80] developed an in situ Raman monitoring system to study interfacial aging in aluminum-filled polydimethylsiloxane (Al/PDMS) composites. By comparing the Raman spectra of individual components and the composite, they confirmed the chemical interaction at the interface, evidenced by the complete consumption of the Si-H bond peak at ~2157 cm^{-1} in the composite (Figure 4f,g), which indicated cross-linking without new peak formation or significant shifts. Their results showed a significant decrease in the intensity of Raman peaks during aging, particularly the Si-O-Si peak at 489 cm^{-1}, with the most pronounced reduction occurring at the Al/PDMS interface. Raman imaging further visualized the intensified degradation around the filler, identifying the interface as the most vulnerable region during thermal aging. In summary, this work employs Raman spectroscopy to reveal the chemical mechanism of interfacial aging in Al/PDMS composites at the molecular scale, emphasizing the critical role of the interface as a region sensitive to aging.

To achieve the resolution limits at the nanoscale interface, TERS technology plays an irreplaceable role. This technique enables the localization of Raman signals at the nanoscale or even atomic scale, directly linking localized structures with chemical information. Lee et al. [81] utilized TERS to probe defect-related vibrational modes in monolayer WS_2 at the nanoscale. By correlating TERS mapping with scanning tunneling microscopy (STM) topography, they identified two defect-induced Raman modes, labeled D and D′, which appear alongside a red-shifted A_{1g} mode at defective sites. These spectral features were most prominent in regions with structural disorders, such as sulfur vacancies (V_S). Density functional theory (DFT) calculations confirmed that V_S not only cause the red shift of the A_{1g} mode but also activate the otherwise Raman-inactive D and D′ modes due to symmetry breaking. Comparative Raman imaging using different laser wavelengths excluded strain effects as the origin of these spectral changes. This study demonstrates that TERS can effectively correlate nanoscale structural defects with specific Raman features, providing a molecular-level understanding of interfacial defects in 2D materials. Shao et al. [82] employed a multimodal nanoscopic approach combining TERS and tip-enhanced photoluminescence (TEPL) to investigate atomic diffusion and the resulting localized optoelectronic properties at the interface of lateral bilayer WS_2/MoS_2 heterojunctions. Using TERS mapping with a spatial resolution better than 40 nm, they identified a transition region where the Raman spectra exhibited features of both WS_2 and MoS_2, indicating the formation of a $Mo_xW_{1-x}S_2$ alloy due to atomic interdiffusion. The evolution of Raman peak positions and intensities across the interface allowed them to quantify the diffusion coefficients of W and Mo atoms by applying Fick's second law to the TERS intensity profiles. This study demonstrated that TERS can directly correlate nanoscale stoichiometric variations with localized optoelectronic responses at heterojunction interfaces. Garg et al. [83] utilized TERS under both resonant and non-resonant conditions to characterize the interface of monolayer MoS_2/WS_2 lateral heterostructures with ~50 nm spatial resolution. Their TERS mapping revealed significant heterogeneity in the interface width, varying from below 50 nm to over 600 nm within a single crystallite. The resonant TERS spectra showed composition-dependent low-energy modes (140–220 cm^{-1}) and a defect-related mode that shifted from 455 cm^{-1} in MoS_2 to 433 cm^{-1} in WS_2, linking it to sulfur vacancies and alloy formation. By comparing resonant and non-resonant TERS, they deconvoluted the effects of resonant enhancement and alloy composition, confirming the interfacial region as a graded $Mo_xW_{1-x}S_2$ alloy and highlighting TERS' capability to probe nanoscale compositional and structural disorder at 2D heterointerfaces.

Furthermore, Rahaman et al. [84] employed tip-enhanced photoluminescence (TEPL) spectroscopy to probe charge transfer excitons (CTXs) at the interface of colloidal nanoplatelets (NPLs) and 2D TMDCs ($MoSe_2/WSe_2$). By comparing spectra from individual components with those from the heterostructure, TEPL identified a new, low-energy photoluminescence peak located 50–80 meV below the $MoSe_2$ A-exciton. This peak, absent in the individual component spectra, serves as a direct spectral signature of localized charge transfer excitons (CTXs) formed at the interface. The spatial resolution of TEPL (<20 nm) allowed this CTX emission to be mapped directly to single NPL-TMDC contact points, confirming nanoscale confinement and providing clear evidence of chemical interaction and interfacial charge transfer. Milekhin et al. [85] employed resonant TERS to probe CdSe nanocrystals on plasmonic substrates. Using gap-mode TERS, they achieved nanoscale spatial resolution and observed strong enhancement of the CdSe longitudinal optical phonon mode at ~212 cm^{-1}, including its overtones, under resonant excitation. Comparative spectral analysis revealed new shoulders attributed to surface optical modes and selenium vibrations, confirming surface-sensitive detection. TERS mapping directly correlated the Raman intensity with localized electromagnetic hotspots at nanodisk edges

and pyramid vertices. This demonstrates TERS as an effective tool for analyzing interfacial phonon behavior and local field enhancement at solid–solid interfaces.

3.2. Analyzing Physical and Chemical Reactions at Water–Oil Interfaces

The aqueous-oil interface is ubiquitous in nature and industry, playing a critical role in systems ranging from cell membranes and emulsions to oil extraction, drug delivery, and pollutant migration. This nanoscale region possesses unique physicochemical properties arising from the stark polarity contrast between the two phases: water, a polar solvent that forms hydrogen-bond networks, and oil, a non-polar medium governed by van der Waals forces. This inherent incompatibility drives molecular orientation, particularly for amphiphilic molecules like surfactants and phospholipids, which assemble into monolayers or multilayers at the interface. Consequently, the interfacial region exhibits distinct local properties, such as polarity, dielectric constant, and micro-solubilization capacity, that profoundly influence key processes like molecular adsorption, mass transfer, and charge transfer. Raman spectroscopy has emerged as a powerful tool for the non-destructive analysis of this dynamic environment. It provides critical insights into the molecular composition, structure, and kinetics of the water–oil interface, thereby helping to elucidate how it regulates related physicochemical processes.

A primary focus has been on understanding how proteins and biopolymers interact with lipids at the interface and how this influences emulsion stability. Meng et al. [86] employed Raman microspectroscopy to investigate the interactions between bovine serum albumin (BSA) and different oils (mineral oil or corn oil) at the protein/oil interface. By analyzing difference spectra obtained by subtracting the spectrum of the individual oil or protein from the interface spectrum, they identified specific structural changes indicative of interactions. Their results revealed that BSA underwent conformational changes primarily at the tertiary structure level upon adsorption to the mineral oil interface, as evidenced by a reduced intensity of the tryptophan band at 750 cm^{-1} and a decreased intensity ratio of the tyrosine doublet (I_{850}/I_{830}), suggesting an altered microenvironment for these hydrophobic residues. In contrast, the protein's secondary structure, reflected in the amide I region, remained largely unchanged. Furthermore, the study demonstrated that the oils themselves were affected: mineral oil showed changes in the symmetric (980 cm^{-1}) and antisymmetric (1071 cm^{-1}) CCC stretches of its hydrocarbon backbone, while corn oil's involvement was mediated through its CH_2, CH_3, COOR, and =C–H groups. The work concluded that hydrophobic interactions were the dominant driving force for protein-lipid interactions at the interface, with hydrogen bonding also playing a significant role, and that the specific behavior differed depending on the oil's chemical structure. Building on the understanding of protein-lipid interactions, Niu et al. [87] investigated how the ratio of two biopolymers, ovalbumin (OVA) and gum arabic (GA), influences the stability of oil-in-water emulsion droplets. Their initial macroscopic characterization established that the 1:2 ratio emulsion exhibited superior creaming stability, oxidative resistance, and enhanced viscoelastic properties compared to other ratios (e.g., 1:1 and 1:3). To decipher the underlying cause, they employed Raman spectroscopy, focusing on the C–H stretching region (2800–3100 cm^{-1}) of the lipid phase. As shown in their Figure 5a, the spectral profiles revealed changes in lipid chain packing. The critical insight came from quantifying the intensity ratio of I_{2853}/I_{2880}, which serves as an indicator of lipid acyl chain order. Their analysis demonstrated that the most stable emulsions (at ratios of 1:2 and 1:3) consistently exhibited the lowest I_{2853}/I_{2880} values, indicating a greater degree of lipid chain disorder compared to pure oil or the less stable 1:1 ratio emulsion. This key spectroscopic evidence allowed the authors to conclude that the superior performance at the 1:2 ratio was attributable to the formation of a thick, densely structured OVA/GA

interfacial layer. This layer penetrates and constrains the lipid core, disrupting its native order and thereby forming a more rigid interface that effectively mitigates coalescence and oxidation. Han et al. [88] further dissected the role of the lipid phase by examining how the unsaturation degree of free fatty acids (Oleic OA, Linoleic LA, Linolenic LNA) influences the adsorption and conformation of salt-soluble pork myofibrillar proteins. This study combined interfacial tensiometry, dilatational rheology, and Raman spectroscopy. A critical finding from the Raman analysis of the adsorbed protein layer was a systematic shift in secondary structure: as unsaturation increased from OA to LNA, the α-helix content significantly decreased. This conformational shift towards more extended structures is consistent with greater protein unfolding at the interface when interacting with more unsaturated lipids. Combined with other characterization results, it is evident that lower unsaturation (OA) favors a more ordered, helical protein structure at the interface, forming a robust film, whereas high unsaturation (LNA) induces excessive protein unfolding, rearrangement, and cross-linking, leading to a less effective interfacial membrane and poorer stability.

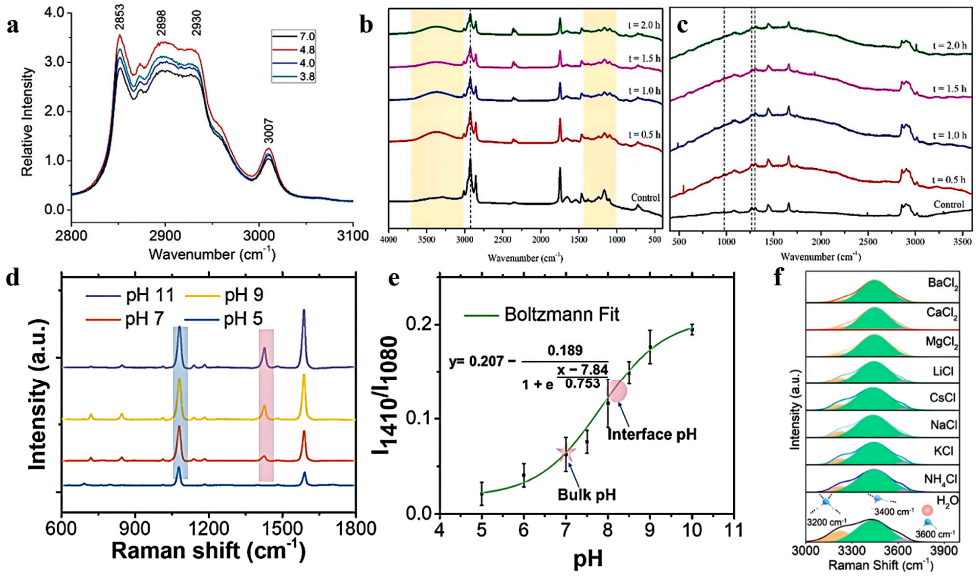

Figure 5. (**a**) Normalized Raman spectra in the 2800–3050 cm^{-1} region from emulsion stabilized by OVA/GA complexes at ratio OVA/GA 1:3, total biopolymer concentration 0.6%, as a function of pH [87]. The (**b**) FT-IR and (**c**) Raman spectra of SPI emulsions treated with protease for 0.5 h, 1.0 h, 1.5 h and 2.0 h [89]. (**d**) SERS spectra were collected at various pH values, where the pink bar is COO^- at 1410 cm^{-1} and the benzene ring at 1080 cm^{-1} in the blue bar. (**e**) A calibration curve was generated by taking the ratio of the height of the peak at 1410 cm^{-1} to that of the peak at 1080 cm^{-1}. The Boltzmann equation was utilized to fit the data [90]. (**f**) Raman spectra of interfacial water in the presence of a series of cations on COOH-SAM surface at pH = 7, and the peak is fitted into three Gaussian subpeaks, representing tetracoordinated water (3200 cm^{-1}), weakly hydrogen-bonded water (3400 cm^{-1}), and free water (3600 cm^{-1}), respectively [91].

Further dissecting the role of bioactive compounds, Hu et al. [92] thoroughly investigated the interfacial complexation between modified goose liver protein (M-GLP) and four hydrophobic polyphenols (curcumin, resveratrol, rutin, and quercetin) at the oil/water (O/W) interface was systematically investigated, with a focus on how hydrophobic interactions influence interfacial stability and polyphenol bioaccessibility. Raman spectroscopy played a role in elucidating conformational changes in the protein and the structural organization of oil droplets. Raman spectral features, such as the decreased intensity ratio of methylene to methyl groups ($I_{2853}/_{2880}$) and alterations in tyrosine and tryptophan microenvironments, indicated improved interfacial packing and a more ordered, dense

protein layer in the presence of curcumin. Complementary interfacial dilatational rheology measurements showed that emulsions containing curcumin exhibited the highest elastic modulus, confirming the formation of a mechanically robust interfacial layer. This enhanced interfacial integrity contributed to superior physical, storage, and photo-stability of the emulsion, as well as improved bioaccessibility of curcumin during in vitro digestion. The study emphasized that polyphenols such as curcumin do not merely enhance emulsion stability through spatial occupancy at the interface. Instead, they modulate protein conformation and interfacial assembly via specific hydrophobic interactions. Similarly, Wang et al. [89] showed that controlled protease hydrolysis induces a specific secondary structural transition in soy protein, leading to a more ordered and stable interfacial layer. They investigated the structural evolution of soybean protein isolate (SPI) at the oil–water interface under controlled protease hydrolysis. Raman spectroscopy was pivotal in quantifying the time-resolved conformational changes in SPI's secondary structure at the interface. The analysis of the amide I band revealed a significant decrease in α-helix content alongside a marked increase in β-sheet and β-turn structures as hydrolysis progressed. Specifically, the content of the β-turn structure peaked at 1.0 h, indicating a more ordered molecular rearrangement facilitated by hydrogen bonding. This specific structural transition, detected directly by Raman, was coherent with FT-IR (Figure 5b,c) findings that suggested the involvement of -CO and -NH groups in electrostatic interactions and hydrogen bonding. Furthermore, intrinsic fluorescence spectroscopy revealed strong fluorescence quenching at this 1.0 h mark, implying that tryptophan residues were buried due to the aggregation and recombination of peptides, thereby altering the protein's tertiary structure. The study concluded that the protease-induced hydrolysis and subsequent recombination of SPI molecules, culminating at the 1.0 h treatment, led to the formation of a more ordered and stable interfacial layer.

Beyond constituent interactions, significant efforts have been directed at characterizing the unique physicochemical properties of the interface itself. Wang et al. [90] utilized surface-enhanced Raman spectroscopy (SERS) to achieve in situ quantitative analysis of the local pH at the oil–water interface. They developed a plasmonic nanosensor by immobilizing the pH-responsive molecule 4-mercaptobenzoic acid (p-MBA) onto gold nanorods (AuNRs). The carboxyl group (–COOH) of p-MBA deprotonates to $–COO^-$ under alkaline conditions, generating a characteristic Raman peak at 1410 cm^{-1}, while the benzene ring peak at 1080 cm^{-1} serves as an internal reference (Figure 5d). By establishing a calibration curve between the intensity ratio (I_{1410}/I_{1080}) and pH (Figure 5e), the local pH was quantitatively determined. Results showed that the pH at the oil–water interface was 8.4 ± 0.4, significantly higher than the bulk value of 7.0. Thermodynamic modeling confirmed that this pH increase did not alter the supersaturation of gypsum, ruling out pH as the governing factor in $CaSO_4$ nucleation. This finding reinforces the proposed mechanism that the negatively charged interface preferentially adsorbs Ca^{2+} ions, enhancing local supersaturation and promoting nucleation, consistent with ICP-MS observations of a Ca^{2+} concentration gradient near the interface. This work provides a direct method for probing the interfacial microenvironment, revealing properties that can differ substantially from the bulk phase and which are crucial for understanding interfacial reactions and stability. He et al. [91] investigated the oil adhesion process on carboxyl-terminated self-assembled monolayer (COOH-SAM) surfaces in ionic solutions and observed the interfacial water structure in this system using SERS (Figure 5f). They found that the lower the tetracoordinate water content, the stronger the oil adhesion. Compared to monovalent ions, the binding of multivalent ions to the COOH-SAM surface was enhanced, leading to more disordered interfacial water and ultimately stronger oil adhesion. The difference in oil adhesion caused by divalent ions was found to be related to the thickness induced by pH-induced interfacial water distur-

bance, i.e., the greater the thickness, the weaker the adhesion force. This study contributes to understanding the mechanisms of superhydrophilicity and adhesion behavior at the molecular level and provides insights into the mechanisms of water-driven oil recovery.

The interfacial water structure was also a key focus for Tomobe et al. [93], who employed a combination of Raman spectroscopy and ab initio molecular dynamics (MD) simulations to elucidate the molecular origin of the blueshift observed in the OH-stretching vibrations of water molecules at the interface of hydrophilic cyclic compounds, specifically six monosaccharide isomers. Using multivariate curve resolution (MCR) analysis of Raman spectra, the authors decomposed the spectral contributions into bulk-like water and solute-correlated (SC) components. In a water molecule, the OH bond that is H-bonded with the monosaccharide is classified as the "near" OH bond, and the opposing OH bond is classified as the "far" OH bond. The SC spectrum revealed blue-shifting in the OH stretching vibration band, with a pronounced blue shift observed in the far-end OH vibration spectrum but not in the near-end OH vibration spectrum (Figure 6a–c). This blue-shift phenomenon was present in all six monosaccharide isomers, indicating that blue-shifting is a fundamental phenomenon common at the interfaces of cyclic compounds. Through ab initio MD simulations, the researchers further analyzed the local hydration environment by distinguishing between "near" and "far" OH bonds of water molecules relative to the monosaccharide oxygen atoms. In this region, water molecules primarily form donor hydrogen bonds with the monosaccharide, leading to a disruption of the tetrahedral hydrogen-bond network. This results in weakly hydrogen-bonded water molecules that exhibit higher-frequency vibrational modes, consistent with the blueshift observed experimentally. The study also introduced a tetrahedral order parameter (TOP) to quantify the local water structure, confirming that the hydration shell in the middle region is structurally perturbed. These findings highlight that the blueshift is not due to the monosaccharide itself, but rather stems from the vibrational behavior of water molecules whose local hydrogen-bonding environment is incompatible with the bulk water network. Taylor et al. [94] employed Raman hyperspectral imaging to directly link the microscopic stability of margarine to its molecular-level hydrogen-bonding network. To objectively analyze the vast spectral dataset, they applied a fundamental unsupervised machine learning algorithm: k-means clustering. This algorithm categorized every pixel in the hyperspectral images based on its entire spectral profile, automatically identifying and mapping distinct chemical regions such as the lipid-rich continuous phase and the water-rich globules, without relying on pre-defined intensity thresholds. To quantitatively decode the complex spectral envelope which arises from the overlapping vibrations of hydroxyl groups in both water and monoacylglycerol (MAG) emulsifiers, they employed a Lorentzian mixture model. As referenced in Figure 6d, this model deconvolutes the broad band into three underlying components, assigned to strong H-bonds (~3275 cm^{-1}), weaker H-bonds (~3457 cm^{-1}), and non-H-bonded OH groups (~3645 cm^{-1}). An H-bonding index (HBI) representing the robustness of H-bonding structure in local water molecules was computed as the sum of the weights of the components of the Lorentzian mixture at 3275 and 3457 cm^{-1}, indicating stronger and weaker H-bonding, respectively (Figure 6e). Combined with other results, it is concluded that a higher average HBI in the oil phase (the lipid matrix outside the water globules) was strongly correlated with reduced oil separation. This demonstrates that the stability of the emulsion is governed not only by the interface but by the robustness of the hydrogen-bonding network permeating the bulk oil phase. Zhang et al. [95] prepared a $CaCO_3$ S/O/W-type emulsion. They compared the intermolecular interactions and solubility characteristics of S/O/W emulsions with different W phases. The results showed that when the W phase was GEL, the S/O/W emulsion was unstable; when the W phase was NaCas or NaCas-GEL, the S/O/W emulsion was stable and had a higher calcium carbonate

content. FTIR, Raman, and XRD analyses indicated that NaCas interacted to some extent with GEL, which was beneficial for the preparation of stable S/O/W emulsions.

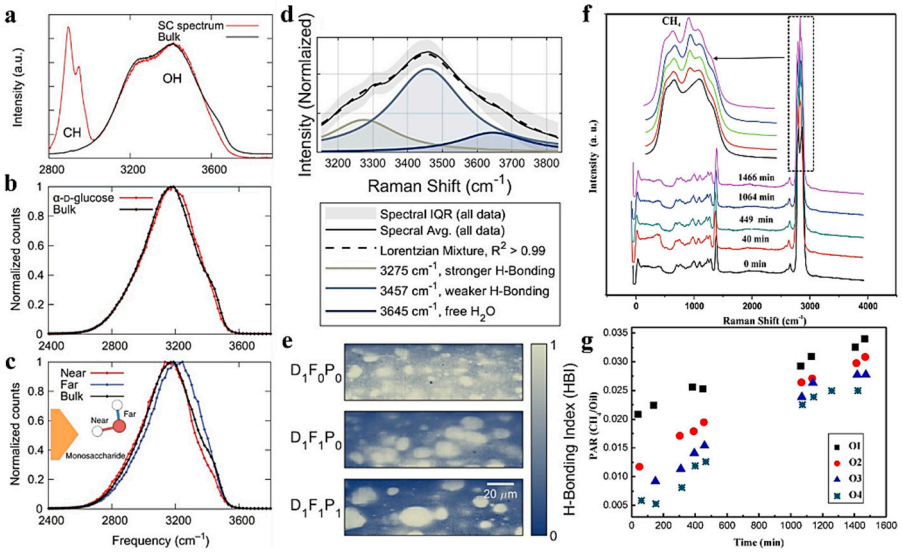

Figure 6. (**a**) Experimental Raman spectrum of the bulk (black line) and SC spectrum (red line). The SC spectrum was obtained using the spectra of D-glucose solutions in 0, 0.05, 0.1, 0.3, and 0.5M. (**b**,**c**) The OH vibrational spectra of water molecules obtained by the Car-Parrinello MD (CPMD) simulations using the wavelet analysis within 3.5 Å of a-D-glucose (red line) (**b**) and near (red line) and far (blue line) OH bonds (**c**). The "near" and "far" represent the OH bonds from the monosaccharide oxygen atoms. a.u., arbitrary unit [93]. (**d**,**e**) Properties of the H-bonding index (HBI) in margarine spreads. (**d**) The average spectrum (solid black line) and the interquartile range (IQR) (shading) over all data in the interval 3100–3835 cm^{-1}, corresponding to water vibrations. A 3-component Lorentzian mixture (dashed black line) is overlaid along with the individual components, having central Raman shifts of 3275 (gray), 3457 (blue–gray), and 3645 (blue) cm^{-1}. (**e**) The areas of the components at 3275 (gray) and 3457 (blue–gray) cm^{-1} were estimated and summed at each pixel, producing the HBI maps. This illustrates the distribution of hydrogen bond intensity across different margarine spreads (e.g., $D_1F_0P_0$, $D_1F_1P_0$, $D_1F_1P_1$, where D, F, and P denote production date, formulation, and manufacturing process, respectively) [94]. (**f**) Temporal evolution of Raman spectra at position OI (within the oil phase, 20 μm from the water–oil interface) during methane diffusion. The increasing intensity of the methane peak (~2910 cm^{-1}) over time (from 0 to 1720 min) indicates the continuous dissolution and diffusion of methane into the oil phase from the vapor phase. (**g**) Changes in the peak area ratio (PAR) of methane to oil at different positions (OI to O4) within the oil phase versus time. The initial significant concentration gradient, evidenced by the disparity in PAR values, gradually diminishes as diffusion proceeds, indicating the homogenization of methane concentration throughout the oil phase prior to hydrate formation [96].

Several studies have leveraged Raman spectroscopy's capability for in situ monitoring of dynamic interfacial processes. Guo et al. [96] employed in situ confocal Raman spectroscopy within a high-pressure optical capillary to directly visualize and quantify the molecular-scale events at the water–oil interface during methane hydrate formation and dissociation. By tracking characteristic Raman peaks of methane (Figure 6f), they mapped methane concentration distributions (Figure 6g), revealing the proportions of CH_4 at different locations within the oil phases (the proportion in the water phase was obtained using the same method). This reflects changes in CH_4 concentration at various positions during diffusion through both phases. This indicates that prior to hydrate formation, methane dissolves from the high-pressure gas phase, rapidly reaching high-concentration saturation in the oil phase. It then slowly diffuses through the oil–water interface into the aqueous phase, forming a concentration gradient from the interface to the interior of the

aqueous phase. This result systematically visualizes and quantifies the process of methane concentration diffusion over time in both oil and water phases, ultimately reaching equilibrium, providing a foundation for subsequent analysis of hydrate formation. Their work addressed a critical industrial problem: how hydrate formation can destabilize emulsions, leading to blockages in pipelines and drilling fluids. Gia et al. [97] successfully prepared silver octahedral plasmonic colloidal particles with SERS properties and applied them to the protonation reaction of dimethyl yellow (DY) at the n-decane–water interface in ultra-small droplets (<200 pL). This enabled in situ monitoring of the reaction process. Xiong et al. [98] combined Raman spectroscopy with stimulated emission fluorescence (SREF) microscopy, enabling fluorescence excitation spectroscopy to map Raman line shapes of vibrational modes with extremely high sensitivity (up to the single-molecule level). This technique can be used to measure the relationship between Raman vibrations at the water–oil interface of droplets and electric fields. The study suggests that the formation of electric fields may be due to charge separation caused by the adsorption of negative ions at the water–oil interface of droplets. This strong electric field may partially explain the unique properties of chemical reactions in droplets. Furthermore, Argyri et al. [99] used acoustic levitation to suspend water droplets in contact with hexadecane droplets and observed the propagation of interfacial crystallization from the hexadecane/water interface throughout the entire hexadecane droplet. Combining acoustic levitation with Raman spectroscopy enables real-time characterization of phase transitions, demonstrated the presence of alkane solid crystals during water evaporation. This study provided insights into the hexadecane interfacial crystallization process and demonstrated the applicability of acoustic suspension for studying non-contact interfacial phenomena between two immiscible liquids.

3.3. Tracking Species Evolutions at Electrochemical Interfaces

The electrochemical interface can also be described as an electrode/solution interface. Raman spectroscopy has been widely used to analyze electrocatalytic processes due to the advantages of high efficiency, ease of detection, and the possibility of monitoring low-wavenumbers species while greatly excluding the influence of solvent water [17]. It is capable of resolving the structure of the electrode/electrolyte interface (bilayer, interfacial water structure), identifying and tracing the intermediates of electrocatalytic reactions (Hydrogen Evolution Reaction HER, Oxygen Evolution Reaction OER, Oxygen Reduction Reaction ORR, Nitrogen Reduction Reaction NRR, etc.) in real time, as well as revealing the conformational relationship between the catalyst surface structure (defects, crystalline surfaces, ligand environments) evolution and reaction activity/selectivity.

3.3.1. Coupling of SERS with In Situ Electrochemical Techniques

As described earlier in Section 2, surface-enhanced Raman spectroscopy has high surface sensitivity and can effectively provide fingerprint structure information of reaction intermediates. Moreover, since the Raman scattering cross-section of water molecules is not large, water interference can be avoided in aqueous systems. Therefore, SERS can be said to be an effective tool for the in situ study of catalytic reaction mechanisms and conformational relationships [37]. Traditionally, electrocatalytic reaction processes and mechanisms have been explored using electrochemical methods, but these methods have inherent limitations. For example, electrical signals cannot chemically identify specific molecules and reveal individual bonding information and fine molecular structures. Therefore, in situ probing of interfacial substances, including the chemical state of the electrocatalyst surface, intermediates, interfacial water/solvents, cations, anions, and the interactions of these factors at the molecular or atomic level, is of great importance to reveal the structure–activity relationships and elucidate the reaction mechanisms. Raman spectroscopy typically covers

a wavenumber range of 100 to 4000 cm^{-1}, which is widely used for detecting oxygen, hydroxyl, and metal–adsorbate bonds in the low-wavenumber region, as well as interfacial water in the high-wavenumber region. These are key interfacial species involved in electrocatalytic reactions [13,100]. It should be noted that the actual measurable spectral range depends on the specific spectrometer and application, with some advanced instruments capable of extending from around 50 cm^{-1} to as high as 8000 cm^{-1}. By in situ Raman spectroscopy, it is possible to address issues such as catalyst reconfiguration, surface adsorbates and reaction intermediates, and the mechanistic role of electrolytes [101].

In 1973, Fleischmann et al. [102] reported the first work using in situ electrochemical Raman spectroscopy for surface/interface studies. In situ electrochemical Raman spectroscopy was utilized to study thin films of HgO deposited on the surface of Pt electrodes, as well as metal halide $HgCl_2$ and $HgBr_2$ films. Since the oxides and halides of Hg can be detected with very strong Raman scattering signals, they can be used to study the reactive kinetic processes on metal electrode surfaces. SERS, as an advanced version of conventional Raman spectroscopy, has gained significant improvements in surface sensitivity and selectivity, further expanding its applications in electrocatalysis. In the mid-1990s, important progress was made in the electrochemical surface-enhanced Raman spectroscopy (EC-SERS), by which a large number of surface Raman enhancements could be assigned to VIII B transition metals of electrochemical and catalytic importance. Molecular level studies of various adsorbates on electrodes of various materials by Raman spectroscopy have been realized [103].

Briefly, EC-SERS technique combines the molecular structure detection capability of SERS with the potential control capability of electrochemistry (Figure 7). By modulating the potential, molecular vibrational information can be obtained along with the behavioral information of the electrochemical reaction, which can then be used to study the formation, transformation, and consumption processes of the reaction intermediates and to reveal the potential-dependent behavior of the catalyst surface species. This technique provides detailed, comprehensive and reliable direct evidence for elucidating electrocatalytic reaction mechanisms at the molecular or atomic level [100].

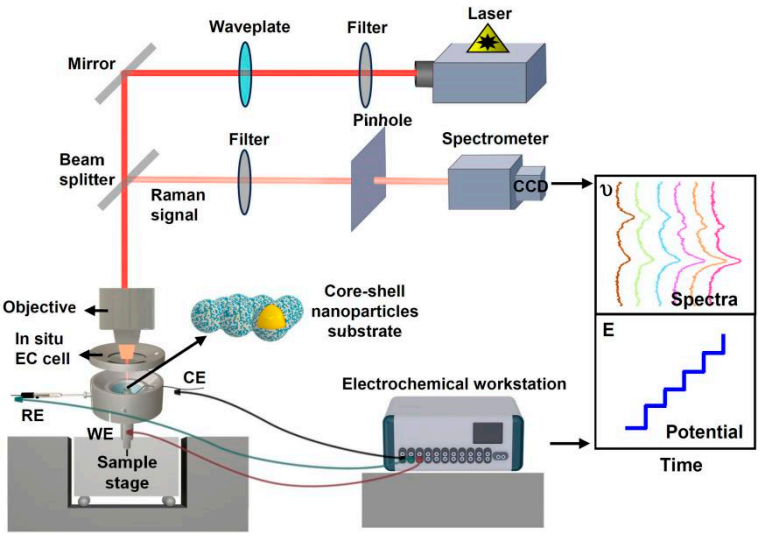

Figure 7. Optical path configuration of in situ EC-SERS. WE: working electrode, RE: reference electrode, CE: counter electrode, CCD: charge-coupled device [100].

3.3.2. Analyzing Catalytic Reactions by Electrochemical Raman Spectroscopy

Interfacial water has rich and complex properties and plays an important role in chemistry, biology, geology and engineering [104]. Electrocatalysis as one of the important

interfacial sciences, has its reaction site at the electrode-solution interface, and interfacial water molecules tend to participate in the vast majority of the electrocatalytic reaction processes. HER as a classical electrochemical reaction of fundamental scientific significance, involves the direct participation of water molecules in its reaction process. An in-depth understanding of the behavior and activity of interfacial water through in situ Raman spectroscopy will explore the true active site and reveal the mechanism of HER [105].

Water molecules as a specific weakly adsorbed species, interact with electrolyte ions through a hydrogen bonding network that extends over multiple water layers. As described in the SERS mechanism section, SHINERS can be used directly on single-crystal surfaces with atomically flat structures. Therefore, SHINERS is considered to be an ideal tool to study interfacial water adsorption on single-crystal surfaces, which can be used to investigate the interfacial dynamics processes on various single-crystal surfaces and to reveal the mechanisms of important interfacial processes [37].

Li et al. [106] combined in situ Raman spectroscopy and ab initio molecular dynamics (AIMD) to study interfacial water at Au single-crystal electrodes under bias potentials. They observed three types of interfacial water molecules undergoing conformational changes with different potentials: as the potential shifted negatively, the interfacial water molecules evolve from structurally "parallel" to "one-H-down" and then to "two-H-down" (Figure 8a). Subsequently, Wang et al. [107] extended the in situ study of interfacial water structure and dissociation to the surface of Pd single crystals using the same technique. The study found that under HER potential, interfacial water undergoes dynamic structural changes, transitioning from random distribution to ordered arrangement, which is facilitated by the bias potential and Na^+ ions. This ordered interfacial water structure promotes efficient electron transfer at the interface, thereby enhancing the HER rate. As shown in Figure 8b, the broad peak at 3000–3800 cm^{-1} is attributed to different configurations of interfacial water molecules, namely 4-coordinated hydrogen-bonded water (4-HB·H_2O, 3155 cm^{-1}), 2-coordinated hydrogen-bonded water (2-HB·H_2O, 3350 cm^{-1}), and Na^+ ion hydrated water (Na·H_2O, 3540 cm^{-1}). The spectral band of the HOH bending mode of water shifts toward lower red wavelengths as the potential decreases, indicating weaker hydrogen bonding interactions between interfacial water molecules at negative potentials. The intensity of the ~550 cm^{-1} spectral band is closely related to the orderliness of the interfacial water structure. As the potential decreases, the intensity of the ~550 cm^{-1} band increases, suggesting that the interfacial water has formed a special ordered structure. The schematic diagram of water dissociation on a Pd single crystal electrode (Figure 8e) demonstrates that Na^+ ions continuously transport water molecules to the interface, reducing the distance between Pd-H bonds and thereby promoting water molecule dissociation (Volmer step). The ordered Na·H_2O structure enhances interfacial electron transfer efficiency, further accelerating HER kinetics. To better understand the regulatory mechanism of cations on interfacial water, You et al. [108] investigated the behavior of interfacial water on a Pd surface in different cation electrolytes (Li^+, Na^+, K^+, Ca^{2+}, Sr^{2+}). As shown in Figure 8c,d, by comparing different cation electrolyte systems, it was found that at a given potential, the frequency of the interfacial water peak increases in a specific order: $Li^+ < Na^+ < K^+ < Ca^{2+} < Sr^{2+}$. High-valent/large-radius cations (such as Sr^{2+}) attract more water molecules to form cation-bound water (M·H_2O), which has weaker hydrogen bonding interactions, resulting in better HER activity. In general, by adjusting the cation radius, valence and concentration, the interfacial water can be made to form a "two-H-down" structure. This unique interfacial water structure can improve the charge transfer efficiency between water and the electrode, further enhancing HER performance.

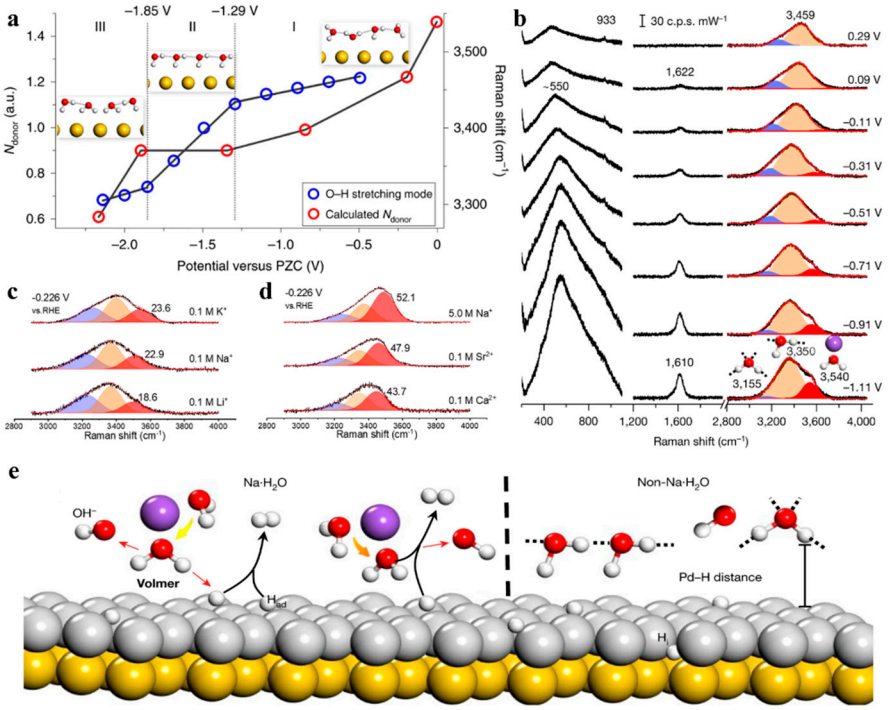

Figure 8. (**a**) Potential-dependent evolution of the hydrogen-bond network of interfacial water [106]. (**b**) In situ Raman spectra of interfacial water on a Pd(111) electrode in a 0.1 M $NaClO_4$ solution (pH 11). Gaussian fits of three O−H stretching modes are shown in blue, orange and red, respectively. c.p.s., counts per second [107]. (**c**,**d**) population of interfacial water in 0.1 M $MClO_4$ (pH 12, M = Li^+, Na^+, K^+, Ca^{2+}, and Sr^{2+}) and 5.0 M $NaClO_4$ (pH 12) electrolytes from in situ Raman spectra [108]. (**e**) Schematic showing interfacial water dissociation on a Pd(111) surface (Au(111) coated with Pd monolayer) [107].

As is well known, platinum (Pt)-based catalysts exhibit high catalytic activity due to their low hydrogen binding energy, enabling them to demonstrate superior performance in the HER. To reduce costs, efforts have been made to lower Pt concentration by using Pt clusters, alloys, and single-atom catalysts. Shen et al. [109] employed Pt-Ni nanoparticles and demonstrated via in situ Raman spectroscopy that the pH-dependent kinetics on the Pt surface and the Ni-induced high activity are driven by the structure of interfacial water. Zhao et al. [110] used organic substrates with structures similar to those of caffeine to investigate the effects of different molecular fragments of caffeine on the alkaline hydrogen oxidation and evolution reactions (HOR/HER) activity on the Pt surface. The study found that the imidazole ring anchors the caffeine molecule to the Pt surface, while the methyl group influences activity by regulating the structure of interfacial water. In situ surface enhanced infrared absorption spectroscopy (SEIRAS) indicated that 7-n-butyltheophylline specifically adsorbed onto the Pt surface. In situ Raman spectroscopy (Figure 9a,b) revealed the presence of weak hydrogen-bonded water characteristic of theophylline-modified Pt surfaces. The intensity of the Raman features increases as the carbon number of the alkyl chain increases from 1 to 4, then decreases as the carbon number increases to 6. Ultimately, it is concluded that weak hydrogen-bonded water plays a key role in enhancing catalyst activity by promoting solvent rearrangement during heterogeneous electron transfer processes. However, organic additives typically introduce steric hindrance, which impedes mass transfer across the Pt surface. To address this issue, Zhou et al. [111] developed an organic 3D porous cage modifier to eliminate interference from surface adsorption or steric effects. In situ electrochemical SERS (Figure 9c,d) and AIMD simulation results indicate that the interaction between the cage and interfacial water primarily occurs via

the cage's -NH- unit, which reduces the rigidity of the interfacial water hydrogen bond network at negative HER potentials, making it sufficiently flexible for rearrangement and improved charge transfer. The -NH- unit acts as an H^+ pump and transfers the formed OH- by forming and breaking H- bonds with interfacial water. Thus, a reactive water layer can be continuously regenerated on the Pt surface. This successfully enhances the rate of the Volmer step at high pH values.

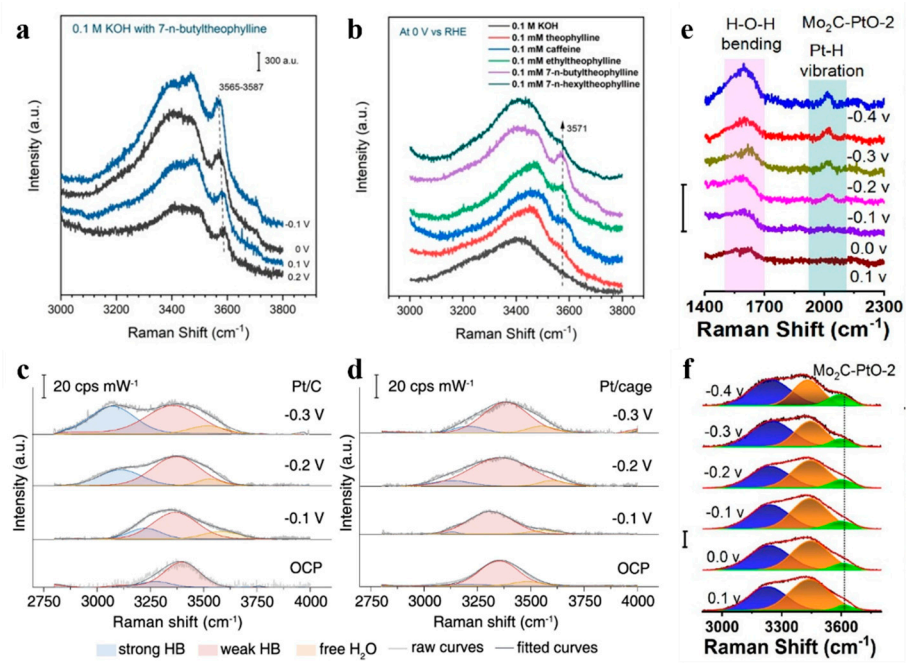

Figure 9. (**a**,**b**) Raman spectra of interfacial water on a pc Pt electrode in 0.1 M KOH with 0.1 mM 7-n-butyltheophylline at −0.1 to 0.2 V, and with 0.1 mM various theophylline derivatives at 0 V. Scale bars represent the Raman intensities [110]. (**c**) In situ electrochemical SERS spectra of the O-H stretching vibrational mode of Pt/C in 0.1 M KOH (HB refers to H-bonds, OCP refers to open circuit potential, cps refers to counts per second). (**d**) In situ electrochemical SERS spectra of the O-H stretching vibrational mode of Pt/cage in 0.1 M KOH [111]. (**e**) In situ Raman scattering spectra of the alkaline HER process for different overpotentials of Mo_2C-PtO-2. (**f**) In situ Raman spectra of interfacial water on Mo_2C-PtO-2 in 0.1 M NaOH (pH = 13), with the Gaussian fits illustrating the three O-H stretching modes in blue (4-coordinated hydrogen-bonded water), orange (2-coordinated hydrogen-bonded water) and green ($Na^+ \cdot H_2O$) [112].

Xiang et al. [112] prepared ultra-thin two-dimensional Mo_2C nanosheets loaded with PtO clusters using a molten salt method combined with a simple liquid-phase deposition technique. Subsequently, in situ Raman spectroscopy (Figure 9e,f) and density functional theory (DFT) simulations demonstrated that the rapid migration of hydrated cations toward the interface and the high adsorption energy of OH* on Mo_2C are key factors in the adsorption and dissociation of water at this interface. Additionally, the interaction between Mo_2C and PtO optimized the adsorption affinity of H* on the PtO catalyst, thereby accelerating HER activity through the kinetically fast Volmer-Tafel pathway. Cao et al. [113] used in situ Raman spectroscopy to monitor the dynamic surface changes and intermediate products of $Pt_1/Ni(OH)_2$, Pt_1/Fe_2O_3 and Pt_1/Mn_3O_4 in alkaline HER in real time. As shown in Figure 10a–c, a H-O-H bending vibration peak was detected in the 1600–1630 cm^{-1} range, corresponding to the presence of adsorbed water. This signal indicates that the $Pt_1/Ni(OH)_2$ surface accelerates the dissociation of water molecules (Volmer step: $H_2O \rightarrow H^+ + OH^-$) and the subsequent desorption of OH^-, significantly enhancing HER kinetics. The characteristic peak at 2030–2100 cm^{-1} is attributed to the vibrational mode of H atoms

coordinated to the Pt surface (ν_{Pt-H}), directly confirming the adsorption and release of H atoms by Pt single atoms as active sites, providing direct spectroscopic evidence for the active center of single-atom catalysts. Through Gaussian fitting of the O-H stretching vibration mode (ν_{O-H}), three types of interfacial water were found on the $Pt_1/Ni(OH)_2$ surface: four-hydrogen-bonded water (4-HB-H_2O), two-hydrogen-bonded water (2-HB-H_2O), and K^+-coupled water (K-H_2O). Additionally, OH radicals were detected at 3600–3660 cm^{-1}, and their strong hydrogen bonding promoted H^+ adsorption, increased the surface hydrogen coverage, and thus optimized the reaction activity. OH radicals were not observed in the in situ Raman spectra of Pt_1/Fe_2O_3 and Pt_1/Mn_3O_4, indicating that the unique electronic structure of $Pt_1/Ni(OH)_2$ (high electronic defect state) and strong orbital hybridization with the $Ni(OH)_2$ carrier (overlap of Pt 3d, Ni 3d, and O 2p orbitals) are key factors in enhancing HER performance.

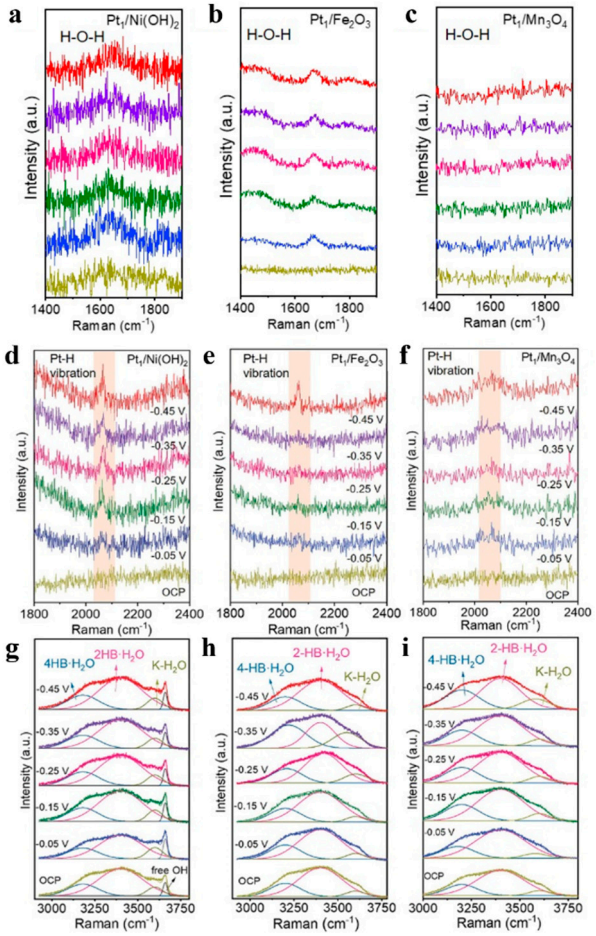

Figure 10. In situ Raman spectra of $Pt_1/Ni(OH)_2$, Pt_1/Fe_2O_3, and Pt_1/Mn_3O_4 at (**a**–**c**) 1400–1900 cm^{-1}, (**d**–**f**) 1800–2400 cm^{-1} and (**g**–**i**) 3000–3750 cm^{-1}, respectively [113]. In the (**a**–**c**), the spectra from bottom to top correspond to applied potentials of open circuit potential (OCP), −0.05 V, −0.15 V, −0.25 V, −0.35 V, and −0.45 V, respectively.

In the water splitting process, in situ identification of active sites is key to accurately regulating the structure of catalytic materials and thereby improving catalytic performance. Recently, the Li research group [114] utilized a borrowing strategy to achieve in situ SERS studies of the reaction process and intermediates of OER on MnO_2-IrO_x with excellent activity. This work constructed Au@MnO_2-IrO_x nanoparticles by growing MnO_2-IrO_x on the surface of Au nanoparticles to detect intermediate species and molecular information. From the in situ enhanced Raman results (Figure 11a), it was observed that the Raman

peak appeared at 1062 cm^{-1} when the potential reached 1.4 V and blueshifted to 1070 cm^{-1} as the potential increased to 1.7 V. Combined with the results of the isotope experiments, it was assumed that the peak was attributed to the superoxide ion *O-O^{-}. The signal at 749 cm^{-1} was confirmed to belong to the *O substance adsorbed on Ir oxide based on the same isotope exchange method (Figure 11b). Combined with the in situ SERS results from DFT simulations, it was found that Au@MnO_2-IrO_x can adsorb *O at lower potentials and saturate rapidly before OER, which facilitates the formation of the superoxide intermediate *O-O. However, the slower adsorption of *O by Au@Ir at the initial OER potential resulted in poorer OER activity. The SHINERS satellite strategy is also a versatile method for understanding catalytic reactions. Dong et al. [115] conducted in situ Raman spectroscopic studies of a-NiO_x/α-Fe_2O_3 using shell-isolated nanoparticles (SHINERS), and a Raman spectral peak located at 701 cm^{-1} in the range of 0.3 V–0.35 V was found (Figure 11c). It was hypothesized from literature reports that this peak might be consistent with the intermediate species *OH. To confirm this hypothesis, deuterium isotope experiments were carried out and the peak was found to be red-shifted to 665 cm^{-1}, indicating that the species is associated with hydrogen atoms. Structural modeling by DFT calculations further suggests that *OH adsorbed on the Ni-site vibrates at 685 cm^{-1}, which is consistent with the in situ Raman results. This information is crucial for understanding the reaction mechanisms and catalyst behavior in electrochemical processes.

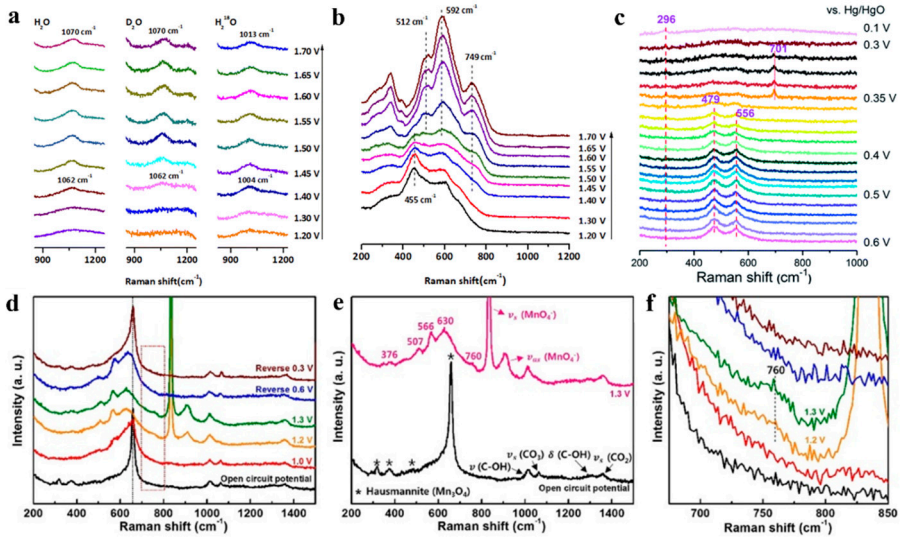

Figure 11. (**a**,**b**) In situ Raman spectra of OER on Au@MnO_2-IrO_x and Au@Ir, respectively [114]. (**c**) In situ SHINERS-satellite spectra of the OER for a-NiO_x/α-Fe_2O_3 [115]. (**d**) Potential-dependent Raman spectra upon increasing the applied potential from open circuit potential (OCP) to 1.3 V and at reversely applied 0.6 V and 0.3 V in 1 M $KHCO_3$ electrolyte. The black dotted line indicates the reversible phase recovery of the initial Mn_3O_4 and the red dotted region demonstrates the evolution of the broad peak at 760 cm^{-1}, respectively. (**e**) Comparison of the Raman spectra collected at OCP and 1.3 V. (**f**) Magnified spectra of the red dotted region depicted in Figure 11d. The peak at 760 cm^{-1} shows the potential-dependent evolution during the water oxidation reaction [116].

In situ capture of structural information about key intermediates can effectively distinguish the active sites and mechanisms of OER and HER processes. Cho et al. [116] identified water oxidation intermediates on the surface of Mn_3O_4 nanoparticles in OER at neutral pH using in situ Raman spectroscopy. In situ Raman spectroscopy measurements revealed reversible phase transitions between Mn_3O_4 and higher-oxidation-state Mn oxide phases (δ-MnO_2), as well as the evolution of a new broad peak centered at 760 cm^{-1} (Figure 11d–f). Combining the potential dependence of the 760 cm^{-1} peak, ^{18}O isotope shift, and scav-

enger consumption analysis confirmed that Mn^{IV}=O is the surface intermediate in the OER. This ultimately revealed the mechanism by which nano-Mn_3O_4 generates Mn^{IV}=O via the Proton-Coupled Electron Transfer (PCET) pathway. Hu et al. [117] used CoO_x as a model catalyst to investigate the synergistic effect of Co_{Td}^{2+} and Co_{OH}^{3+} active sites in the electrocatalytic oxygen evolution reaction. In situ SERS (Figure 12a–c) was used to study the formation and evolution of reaction intermediates on the catalyst surface during the OER process. Based on the surface-enhanced Raman spectroscopy results from ion exchange experiments, it was concluded that Co_{OH}^{3+} serves as the catalytic center for the conversion of OH^- to the O-O^- intermediate (1140–1180 cm^{-1}). Ram et al. [118] found that by controlling the oxygen evolution reaction through regulating the interfacial water structure and intermediate species in the delaminated cobalt tungstate (CWO-del) lattice, proton exchange membrane water electrolysis can be made active and stable. In situ Raman spectroscopy at 1.7 V vs. Reversible Hydrogen Electrode (RHE) revealed new oxide peaks, some of which are not visible in non-in situ Raman spectroscopy (Figure 12e). These new peaks correspond to layered β-CoOOH (~502 cm^{-1}), γ-CoOOH (~571 cm^{-1}), higher-oxidiation Co^{IV}-O (~840 cm^{-1}), and Co-peroxide (~1080 cm^{-1}). To gain a deeper understanding of the peroxide species and the nature of the active sites, additional in situ Raman spectroscopy studies were conducted before and after the onset potential of the OER (Figure 12d). The peak intensities of β-CoOOH and Co-peroxide increased steadily from the open-circuit potential (OCP) to 1.9 V (vs. RHE) and disappeared as the potential was cycled back to OCP from 1.9 V (vs. RHE). This confirms that CWO-del forms higher-oxidiation Co^{IV}-O and Co-peroxide active sites in situ under OER conditions, which serve as the structural basis for its high catalytic activity.

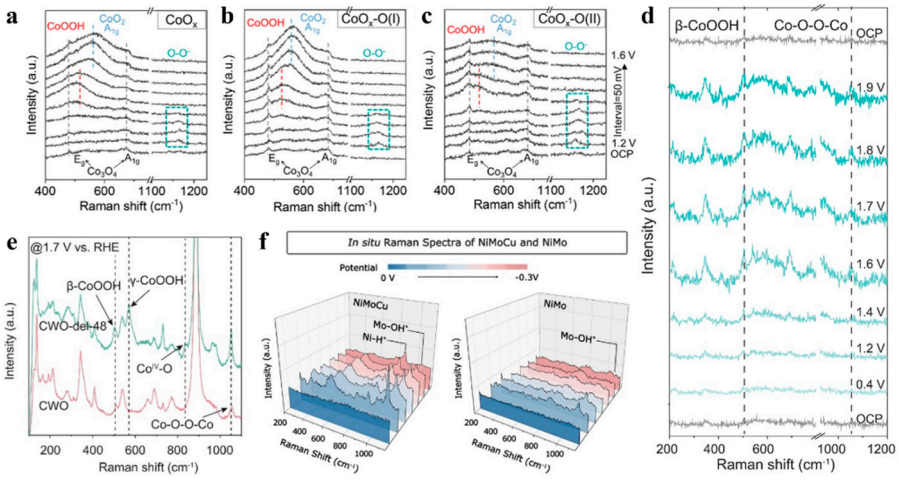

Figure 12. (**a**–**c**) In situ SERS spectra of the OER process on CoO_x, CoO_x-O(I), and CoO_x-O(II) NPs in a 1.0 M KOH solution [117]. (**d**) Operando Raman spectra of CWO-del-48 (on carbon paper, from OCP to 1.9 V versus RHE in 0.5 M H_2SO_4). (**e**) In situ Raman spectra of CWO and CWO-del-48 catalysts at 1.7 V versus RHE suggests the involvement of Co (III), Co (IV), and Co-peroxide as the active OER species [118]. (**f**) In situ Raman spectra of NiMoCu and NiMo during the HER [119].

Zhou et al. [119] addressed the bottleneck issue of alkaline HER by developing a ternary NiMoCu alloy catalyst. In situ Raman spectroscopy revealed the competitive adsorption of the adsorbed intermediates H* and OH*. In the Raman spectrum of NiMoCu, Raman peaks corresponding to the Ni-H* (888 cm^{-1}) and Mo-OH* (1059 cm^{-1}) bonds were observed (Figure 12f), indicating that the introduction of Cu induced the segregation of H* and OH* adsorption sites in the NiMo alloy catalyst, thereby promoting the cleavage of the H-OH* bond. As the overpotential increases, the intensity ratio of the peak representing Ni-H* to that of Mo-OH* increases, indicating an increase in the coverage of effective H*

intermediates, enhanced desorption of OH* in the NiMoCu catalyst, and accelerated HER process. DFT results further confirm that the presence of MoO_4^{2-} on the NiMoCu surface optimizes H* adsorption at the Ni-Cu bisite.

Understanding the surface activity centers and reaction mechanisms of electrocatalytic materials remains one of the hotspots and challenges in catalysis research. Further studies are expected to provide a better understanding of the activity and selectivity of catalytic materials as well as their dynamic conformational relationships, which in turn will provide more in-depth guidance for the design and synthesis of efficient catalysts.

3.4. Raman Spectroscopy Combined with Data Processing to Analyze Interface Substances

Raman–MCR is a powerful chemometric method that combines Raman spectroscopy with multivariate curve resolution (MCR). Its core objective is to extract the Raman spectra of pure components from complex Raman data, which typically contain multiple chemical components with overlapping spectral signals, and to determine their concentration distributions in the sample as a function of space (imaging) or time (dynamic processes).

A prominent application of Raman–MCR lies in elucidating the structure and dynamics of hydration shells at molecular interfaces. Scheu et al. [120] employed Raman multivariate curve resolution (Raman–MCR) to isolate solute-correlated (SC) spectra from Raman data, thereby probing the hydration shells of octylsulfate (OS^-) and octyltrimethylammonium (OTA^+) ions in aqueous solutions below their critical micelle concentrations. The SC spectrum of OS^- (Figure 13a) exhibited an intense OH-stretch band, likely arising from the hydrogen-bonded interaction between the OH group of water molecules and the head group of the sulfate anion. Similar SC OH bonds are observable in the hydration shell spectra of halide anions and share identical characteristics with the SC spectrum of sulfate ions in aqueous solution. In contrast, the SC spectrum of OTA^+ exhibits a double peak characteristic at approximately 3250 and 3450 cm^{-1}, alongside a free hydroxyl peak at 3660 cm^{-1}. This pattern mirrors previously observed hydration shells around nonpolar groups, such as the hydration structures of hydrophobic solutes like alcohols and tetraalkylammonium ions. This indicates that the cationic head groups undergo weaker and more hydrophobic hydration interactions. These spectral differences reflect the distinct nature of water interactions with anionic and cationic headgroups: anionic headgroups are stabilized on the aqueous side through strong hydrogen bonding, while cationic headgroups exhibit hydrophobic-like behavior, favoring closer proximity to the oil phase. Further investigations using second harmonic scattering (SHS) and vibrational sum frequency scattering (SFS) confirmed that the two types of surfactants also differ significantly in their arrangement at the oil/water interface and their influence on interfacial water structure and oil chain ordering, thereby revealing their distinct roles in interface stabilization mechanisms. Building on the theme of ionic effects, Judd et al. [121] further quantified the influence of H^+, OH^-, and salts on hydrophobic self-assembly using Raman–MCR combined with multi-aggregation chemical potential surface (MCPS) analysis. They discovered that while OH^- and common salt ions are expelled from the hydration shell of oily molecules (promoting salting-out and higher-order aggregation), H^+ is uniquely attracted to it. This affinity of H^+ nearly cancels the salting-out effect of its counter-anion, providing direct spectroscopic evidence for a negative charge at molecular oily interfaces and highlighting the ion-specific effects that govern hydrophobic interactions.

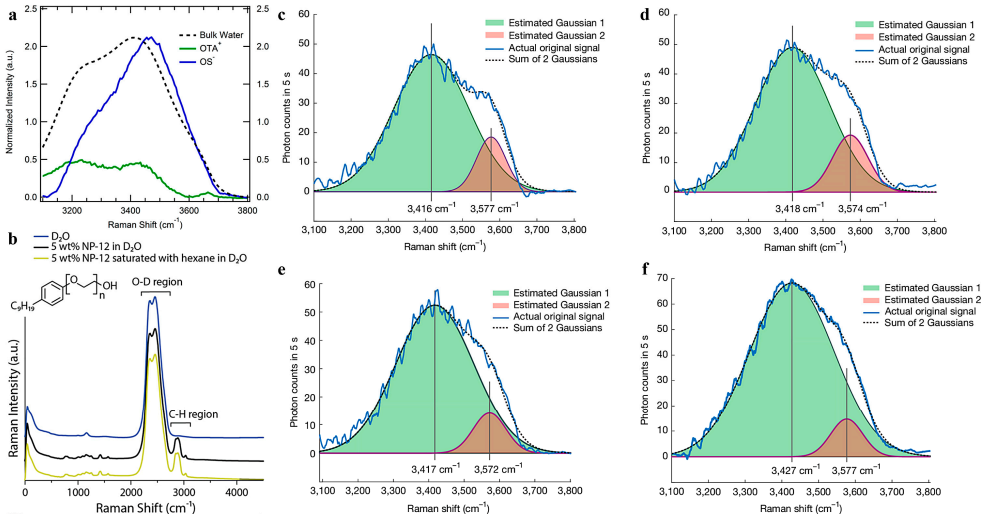

Figure 13. (**a**) Amphiphile ion hydration. SC (hydration-shell) spectra of octylsulfate ions (OS^-) and octyltrimethylammonium (OTA^+) ions obtained using Raman–MCR. The solute-correlated spectra are normalized to the respective CH stretches of the surfactant ions, displaying the OH-stretch vibrational response of water surrounding the surfactant ions. The black dashed line depicts the OH Raman band of bulk water (scaled to the same height as the OS^- hydration-shell OH band) [120]. (**b**) Overlayed artificially spaced Raman spectra of pure D_2O (blue line), 5 wt% Tergitol NP-12 micelles in D_2O (black line), and 5 wt% Tergitol NP-12 micelles saturated with hexane (yellow line). Tergitol NP-12 structure is shown where *n* is an average of 12 [122]. (**c**,**d**) SC spectra (blue) fitted by Gaussian profiles for replicates of 1% d34-hexadecane droplets in water. (**e**,**f**) SC spectra (blue) fitted by Gaussian profiles for replicates of 2% regular hexadecane droplets in water (**e**) and 2% d34-hexadecane droplets in water [104].

The structural transformation of water at hydrophobic interfaces is not only ion-sensitive but also exhibits a strong dependence on temperature and length scale. Davis et al. [123] systematically mapped this transformation using polarized, isotopic, and temperature-dependent Raman–MCR on linear alcohols. They observed that at low temperatures, hydration shells possess enhanced tetrahedral order with fewer weak hydrogen bonds. As temperature increases, this ordered structure gives way to a more disordered one for hydrophobic chains longer than ~1 nm, akin to the water structure at an air–water interface. This thermally induced crossover aligns with theoretical predictions and underscores the cooperative nature of hydrophobic hydration. Extending these insights to more complex, curved interfaces, Shi et al. [104] utilized Raman–MCR alongside multiscale simulations to probe water-in-oil emulsion droplets. SC spectral results showed the disappearance of the shoulder peak at 3250 cm^{-1} (Figure 13c–f), indicating that the characteristic peak representing strong hydrogen bonds and tetrahedral order in the SC spectrum had almost vanished, suggesting a weakening of the hydrogen bond network and reduced order at the interface. A new peak at ~3575 cm^{-1} was assigned to the stretching vibration of free hydroxyl groups (free OH), showing a red shift of 95 cm^{-1} compared to the planar oil–water interface (3670 cm^{-1}), which was induced by the strong electric field. Ultimately, it was concluded that the emulsion droplet interface (non-planar or small-molecule interface) exhibits a synergistic effect between weakened hydrogen bonding networks and strong electric fields, which is a key factor in accelerating microdroplet chemical reactions.

Beyond molecular solvation and ionic solutions, Raman–MCR proves equally potent in deconvoluting spatial distributions within matter and biological assemblies. Wentworth et al. [122] demonstrated this by investigating oil solubilization in nonionic micelles. By separating the OD stretching vibration peak (2200–2775 cm^{-1}) using deuterium-labeled water (D_2O), they successfully extracted the micelle-disturbed water signal, avoid-

ing interference from the surfactant CH peak (Figure 13b). Changes in the intensity ratio of the π-H bond and free OH peaks (2703/2732 cm^{-1}) revealed that the π-H bond disappears after short-chain oil solubilization (ratio < 1), indicating that oil molecules penetrate into the aromatic ring region, disrupting water–aromatic ring interactions. Long-chain oil retains the π-H bond (ratio≈1.4), suggesting it is confined to the hydrophobic core. This work reveals that the solubilization sites of oil molecules within nonionic micelles exhibit chain-length dependence. Similarly, Hossain et al. [124] achieved direct, label-free quantification and spatial mapping of amylose and amylopectin within single starch granules by integrating Raman micro-spectroscopy with machine learning and semi-supervised MCR. This approach successfully resolved their overlapping spectral features and revealed distinct spatial distributions, amylopectin enriched in the granule center and amylose more prevalent in the periphery, showcasing the method's unparalleled capability for in situ compositional and spatial analysis of complex biomaterials.

4. Challenges of Raman Spectroscopy for Interface Detection

Raman spectroscopy and surface-enhanced Raman spectroscopy have great potential in interfacial resolution due to their high sensitivity and ability to provide molecular fingerprinting information, and are particularly suitable for in situ identification of reaction intermediates, monitoring of interfacial processes, and understanding of reaction mechanisms in aqueous environments. However, its practical application still faces a series of serious challenges that need to be deeply understood and overcome.

4.1. Stability and Design Complexity of SERS Substrates

Under extreme reaction conditions, SERS substrates, which are usually made of plasmonic nanostructures such as gold or silver, may undergo phenomena such as oxidation, dissolution or structural changes, which may lead to signal loss or degradation. To address this problem, core–shell structures (e.g., catalytic material shells@Au cores) or loading catalytic nanoparticles onto SERS active substrates (e.g., Au nanoparticles/arrays) have been designed. However, there are still problems such as shell layer thickness control and interfacial effects. For complex core–shell or loaded structures, it becomes difficult to ensure uniform and reproducible SERS enhancement across the electrode surface. For non-traditional SERS substrates, the enhancement mechanism is mainly based on the chemical enhancement mechanism. Since the CM enhancement factor is usually much lower than that of EM enhancement, the signal is weak and extremely sensitive to the surface state, making it difficult to obtain high-quality spectra stably. Meanwhile, the understanding of CM is much less thorough than that of EM, and the mechanism is complicated to explain, which makes it more difficult to identify the signal source.

4.2. Uniformity and Repeatability of SERS Signals

Since SERS signals originate mainly from "hot spots" formed by plasma nanostructures, their distribution is highly heterogeneous. Therefore, the detected signals may only come from a few highly enhanced points and are not representative of the average situation on the entire electrode surface. This limits the generalizability of the study. In most cases, the active sites of the catalysts themselves may be unevenly distributed due to the different ways in which the substances to be tested are loaded on the substrate. Spatially precise correlation of SERS "hot spots" with catalytic "active sites" is a great challenge. Moreover, the SERS enhancement factor is affected by multiple factors (distance, orientation, local field) and is highly nonlinear. Accurate quantification of SERS signal intensity into surface species concentration or coverage is currently almost impossible. Usually only semi-quantitative or trend analyses can be done.

4.3. Interference of Test Conditions on SERS Signals

Strong Raman scattering by water molecules, the presence of electrolyte ions, and electrode potentials can interfere with the SERS signal. Changes in the electrode potential can significantly affect the redox state of the bilayer structure, adsorbed species, and even the substrate material, leading to drastic, nonlinear changes in the Raman background signal. This brings great difficulties to the extraction and quantitative analysis of weak SERS signals. Certain electrolyte components (e.g., organics, impurities) may produce a strong fluorescence background, which severely interferes or even drowns out the SERS signal. Water molecules and some common electrolyte ions (e.g., SO_4^{2-}, ClO_4^-) can also make the SERS signal relatively weak due to their low Raman scattering cross-section. Electrolyte ions or solvent molecules may strongly adsorb to the active site and compete with the reaction intermediates, affecting the formation, stability and detectability of the intermediates. In addition, the creation, growth and detachment of bubbles can lead to drastic changes in the local environment (concentration, refractive index) and scattering conditions, causing large fluctuations and instability in the SERS signal. When detecting microplastics, antibiotics, and other substances in real samples, the reliability of the intrinsic SERS signal can be reduced due to other substances in the complex medium that can reduce the reliability of the intrinsic SERS signal by contaminating the surface of the substrate or masking the target Raman signal, which can lead to inaccurate quantification [125].

4.4. Inherent Difficulties in the Detection of Electrochemical Reaction Intermediates

During electrocatalytic water splitting, many key reaction intermediates may have very low surface coverage under steady-state reaction conditions. Even if there is an enhancement effect, it is close to or even below the detection limit of SERS. Moreover, the intermediates (especially OER intermediates, e.g., *O, *OOH) tend to be very reactive, and the rates of formation and conversion are usually very fast, leading to extremely short lifetimes. Conventional continuous-wave SERS measurements have insufficient time resolution to capture these transient species. Therefore, the development of an in situ, real-time, high temporal and spatial resolution Raman characterization technique is essential for a comprehensive understanding of the dynamic structure–activity relationship of catalysts [16].

In addition, a wide range of possible adsorbed species are present at the electrode/solution interface, including reaction intermediates, solvent molecules, electrolyte ions, impurities and lattice/surface groups of the catalyst itself. Their Raman peaks may appear to overlap or be close in position. Many putative reaction intermediates are difficult to stabilize on the model system and obtain their standard Raman spectra. Vibrational frequency calculations aided by theoretical calculations are the main means, but the results are affected by generalization and model accuracy leading to some uncertainties. Meanwhile, the vibrational frequencies of the intermediates move as their adsorption configurations and bonding strengths change with the potential, increasing the complexity and uncertainty of the designation. It is a challenge to distinguish whether the Raman shifts are for different species or the same species.

5. Conclusions and Outlooks

Raman spectroscopy, especially SERS, has become a central tool for resolving interfacial reaction mechanisms by virtue of its extremely high surface sensitivity, excellent molecular fingerprinting ability, and in situ real-time monitoring. In this review, the breakthrough progress of this technique in revealing the key processes at interfaces is systematically reviewed. Through dynamic monitoring of molecular configurations (e.g., hydrogen bonding networks, ionic coupling effects) at different interfaces, the conforma-

tional relationship between molecular structure and reactivity is elucidated. Understanding the molecular composition, structure, and kinetic behavior at the water–oil interface can provide significant help in regulating related physicochemical processes. Key intermediates such as *H, *O, *OO in HER and OER were successfully captured and identified, providing direct spectral evidence for the validation of the reaction pathways. The dynamics of the conversion of "pre-catalysts" to real active phases and their intrinsic correlation with catalytic performance have been revealed. These results deepen the understanding of the reaction mechanism at the interface and provide a solid scientific foundation for environmental governance, food safety and rational design of efficient catalysts.

Although Raman spectroscopy and SERS technologies show great potential, their practical applications still face multiple challenges. For the future, the development of this technology needs to focus on the following directions to break through the bottleneck:

(1) Innovative substrate design and material systems: Developing stable SERS substrates with high chemical inertness and wide potential window; and optimizing the shell material and thickness of the core–shell structure, exploring carbon-based or semiconductor enhancement materials, and achieving accurate detection of non-traditional SERS active materials.

(2) Advanced technology integration: Raman is coupled with scanning probe technology (STM/AFM-TERS), X-ray technology (XAS/XPS), infrared spectroscopy (ATR-SEIRAS), mass spectrometry (on-line differential electrochemical mass spectrometry DEMS) and other multi-techniques to provide multi-dimensional information on interfaces and to obtain a comprehensive understanding of the reaction interface.

(3) High-resolution imaging: Using TERS and super-resolution Raman imaging techniques (e.g., SERS-PALM/STORM) to enhance spatio-temporal resolution and signal resolution and the development of ultra-fast time-resolved SERS techniques to capture transient intermediate dynamics; and mapping the chemical composition and reactivity distribution of water interfaces at the nano/molecular scale.

(4) Machine learning and big data: Deeply integrating AI (e.g., deep learning algorithms) for efficient deconvolution of complex spectra and automatic identification and designation of feature peaks, and to enhance the accuracy and efficiency of data analysis; and using AI to process massive in situ Raman spectroscopy data to automatically identify feature peaks, track species concentration, and build spectral-structural-performance prediction models.

(5) Novel reactor design: Developing more compact and versatile in situ/worked Raman reaction cells for extreme conditions.

In conclusion, Raman spectroscopy is leaping from a traditional characterization tool to a high-precision, dynamic and intelligent mechanism research platform. By continuously overcoming technical bottlenecks and deepening multidisciplinary cross-fertilization, Raman spectroscopy is expected to completely depict the dynamic processes of interfacial reactions at the nanometer or even single-molecule scale, and provide precise guidance for interfacial engineering in the fields of energy catalysis, environmental governance and biomedicine.

Author Contributions: Formal analysis, T.W.; investigation, T.W.; data curation, Y.J. and H.F.; writing—original draft preparation, T.W.; writing—review and editing, L.L.; resources, Q.D.; supervision, C.W.; project administration, C.W.; funding acquisition, D.L. and C.W. All authors have read and agreed to the published version of the manuscript.

Funding: This research was funded by the National Natural Science Foundation of China (Grant No. 12574003, 52471250), Beijing Natural Science Foundation (Grant No. L248027 and L245019).

Data Availability Statement: Data sharing is not applicable (no new data is generated).

Conflicts of Interest: The authors declare no conflicts of interest.

References

1. Bao, Y.-F.; Zhu, M.-Y.; Zhao, X.-J.; Chen, H.-X.; Wang, X.; Ren, B. Nanoscale Chemical Characterization of Materials and Interfaces by Tip-Enhanced Raman Spectroscopy. *Chem. Soc. Rev.* **2024**, *53*, 10044–10079. [CrossRef]
2. Björneholm, O.; Hansen, M.H.; Hodgson, A.; Liu, L.-M.; Limmer, D.T.; Michaelides, A.; Pedevilla, P.; Rossmeisl, J.; Shen, H.; Tocci, G.; et al. Water at Interfaces. *Chem. Rev.* **2016**, *116*, 7698–7726. [CrossRef]
3. Wang, X.; Huang, S.-C.; Huang, T.-X.; Su, H.-S.; Zhong, J.-H.; Zeng, Z.-C.; Li, M.-H.; Ren, B. Tip-Enhanced Raman Spec-troscopy for Surfaces and Interfaces. *Chem. Soc. Rev.* **2017**, *46*, 4020–4041. [CrossRef]
4. Xu, S.; Wu, J.; Guo, Y.; Zhang, Q.; Zhong, X.; Li, J.; Ren, W. Applications of Machine Learning in Surfaces and Interfaces. *Chem. Phys. Rev.* **2025**, *6*, 011309. [CrossRef]
5. Sun, W.; Xu, Y.; Zhou, Y.; Zeng, Z.; Wang, L.; Ouyang, J. Topographic Scanning Electronic Microscopy Reveals the 3D Surface Structure of Materials. *Adv. Funct. Mater.* **2025**, *35*, 2420372. [CrossRef]
6. Kiyama, R.; Yoshida, M.; Nonoyama, T.; Sedlačík, T.; Jinnai, H.; Kurokawa, T.; Nakajima, T.; Gong, J.P. Nanoscale TEM Imaging of Hydrogel Network Architecture. *Adv. Mater.* **2023**, *35*, 2208902. [CrossRef]
7. Falsafi, S.R.; Rostamabadi, H.; Assadpour, E.; Jafari, S.M. Morphology and Microstructural Analysis of Bioactive-Loaded Micro/Nanocarriers via Microscopy Techniques; CLSM/SEM/TEM/AFM. *Advances Colloid Interface Sci.* **2020**, *280*, 102166. [CrossRef]
8. Elemans, J.A.A.W. Externally Applied Manipulation of Molecular Assemblies at Solid-Liquid Interfaces Revealed by Scan-ning Tunneling Microscopy. *Adv. Funct. Mater.* **2016**, *26*, 8932–8951. [CrossRef]
9. Mallick, S.; Jena, M.; Das, B.; Mohanty, B.; Patel, B.K.; Das, D.P.; Rath, A. Tuning and Understanding of Layered 2D MoS2 –MoO3 Interface for Enhanced Photocatalytic Activities. *Adv. Funct. Mater.* **2025**, *35*, 2422645. [CrossRef]
10. Wang, J.; Hsu, C.-S.; Wu, T.-S.; Chan, T.-S.; Suen, N.-T.; Lee, J.-F.; Chen, H.M. In Situ X-Ray Spectroscopies beyond Con-ventional X-Ray Absorption Spectroscopy on Deciphering Dynamic Configuration of Electrocatalysts. *Nat. Commun.* **2023**, *14*, 6576. [CrossRef] [PubMed]
11. Zhong, W.; Tao, J.; Chen, Y.; White, R.G.; Zhang, L.; Li, J.; Huang, Z.; Lin, Y. Unraveling the Evolution of Cathode–Solid Electrolyte Interface Using Operando X-Ray Photoelectron Spectroscopy. *Adv. Powder Mater.* **2024**, *3*, 100184. [CrossRef]
12. Chen, M.; Liu, D.; Qiao, L.; Zhou, P.; Feng, J.; Ng, K.W.; Liu, Q.; Wang, S.; Pan, H. In-Situ/Operando Raman Techniques for in-Depth Understanding on Electrocatalysis. *Chem. Eng. J.* **2023**, *461*, 141939. [CrossRef]
13. Hess, C. New Advances in Using Raman Spectroscopy for the Characterization of Catalysts and Catalytic Reactions. *Chem. Soc. Rev.* **2021**, *50*, 3519–3564. [CrossRef]
14. Dodo, K.; Fujita, K.; Sodeoka, M. Raman Spectroscopy for Chemical Biology Research. *J. Am. Chem. Soc.* **2022**, *144*, 19651–19667. [CrossRef]
15. Tittel, J.; Knechtel, F.; Ploetz, E. Conquering Metal–Organic Frameworks by Raman Scattering Techniques. *Adv. Funct. Mate-Rials* **2024**, *34*, 2307518. [CrossRef]
16. Hu, W.; Luo, Y.; Zhu, E.; Zhang, A.; Wang, L. Revealing the Electrocatalytic Reaction Mechanism of Water Splitting by In Situ Raman Technique. *Adv. Sustain. Syst.* **2024**, *8*, 2400387. [CrossRef]
17. Chen, Z.; Fan, Q.; Zhou, J.; Wang, X.; Huang, M.; Jiang, H.; Cölfen, H. Toward Understanding the Formation Mechanism and OER Catalytic Mechanism of Hydroxides by In Situ and Operando Techniques. *Angew. Chem. Int. Ed.* **2023**, *62*, e202309293. [CrossRef] [PubMed]
18. Liu, Z.; Zhang, N.; Xiong, Y. In Situ Raman Characterizations for Enhanced Understandings on Electrocatalysis. *J. Phys. Chem. C* **2024**, *128*, 13651–13665. [CrossRef]
19. Wu, S.; Liang, Z.; Wang, T.; Liu, X.; Huang, S. In Situ Characterization Techniques: Main Tools for Revealing OER/ORR Catalytic Mechanism and Reaction Dynamics. *Inorg. Chem. Front.* **2025**, *12*, 848–875. [CrossRef]
20. Ding, S.-Y.; You, E.-M.; Tian, Z.-Q.; Moskovits, M. Electromagnetic Theories of Surface-Enhanced Raman Spectroscopy. *Chem. Soc. Rev.* **2017**, *46*, 4042–4076. [CrossRef]
21. Zrimsek, A.B.; Chiang, N.; Mattei, M.; Zaleski, S.; McAnally, M.O.; Chapman, C.T.; Henry, A.-I.; Schatz, G.C.; Van Duyne, R.P. Single-Molecule Chemistry with Surface- and Tip-Enhanced Raman Spectroscopy. *Chem. Rev.* **2017**, *117*, 7583–7613. [CrossRef]
22. Zong, C.; Xu, M.; Xu, L.-J.; Wei, T.; Ma, X.; Zheng, X.-S.; Hu, R.; Ren, B. Surface-Enhanced Raman Spectroscopy for Bioa-nalysis: Reliability and Challenges. *Chem. Rev.* **2018**, *118*, 4946–4980. [CrossRef] [PubMed]
23. Li, J.F.; Huang, Y.F.; Ding, Y.; Yang, Z.L.; Li, S.B.; Zhou, X.S.; Fan, F.R.; Zhang, W.; Zhou, Z.Y.; Wu, D.Y.; et al. Shell-Isolated Nanoparticle-Enhanced Raman Spectroscopy. *Nature* **2010**, *464*, 392–395. [CrossRef] [PubMed]
24. Li, J.-F.; Zhang, Y.-J.; Ding, S.-Y.; Panneerselvam, R.; Tian, Z.-Q. Core–Shell Nanoparticle-Enhanced Raman Spectroscopy. *Chem. Rev.* **2017**, *117*, 5002–5069. [CrossRef]

25. Kurouski, D.; Dazzi, A.; Zenobi, R.; Centrone, A. Infrared and Raman Chemical Imaging and Spectroscopy at the Nanoscale. *Chem. Soc. Rev.* **2020**, *49*, 3315–3347. [CrossRef] [PubMed]
26. Raman, C.V.; Krishnan, K.S. A New Type of Secondary Radiation. *Nature* **1928**, *121*, 501–502. [CrossRef]
27. Fleischmann, M.; Hendra, P.J.; McQuillan, A.J. Raman Spectra of Pyridine Adsorbed at a Silver Electrode. *Chem. Phys. Lett.* **1974**, *26*, 163–166. [CrossRef]
28. Albrecht, M.G.; Creighton, J.A. Anomalously Intense Raman Spectra of Pyridine at a Silver Electrode. *J. Am. Chem. Soc.* **1977**, *99*, 5215–5217. [CrossRef]
29. Zhu, Y.-Z.; Zhou, R.-Y.; Hu, S.; Li, J.-F.; Tian, Z.-Q. Shell-Isolated Nanoparticle-Enhanced Raman Spectroscopy: Toward High Sensitivity and Broad Applicability. *Acs Nano* **2024**, *18*, 32287–32298. [CrossRef]
30. Qian, Z.-X.; Zeng, J.-S.; Zhao, S.; Zheng, Q.-N.; Tian, J.-H.; Xu, Q.-C.; Zhang, H.; Li, J.-F. In Situ Exploration of Oxygen Electrocatalysis Using Core-Shell Nanostructure-Enhanced Raman Spectroscopy. *Nano Mater. Sci.* **2024**, *in press*. [CrossRef]
31. Roy, S.S.; Nagappan, S.; Satheesan, A.K.; Karmakar, A.; Kundu, S. Surface-Enhanced Raman Scattering Coupled with In Situ Raman Spectroscopy for the Detection of the OER Mechanism: A Mini-Review. *J. Phys. Chem. C* **2024**, *128*, 13634–13650. [CrossRef]
32. Huang, Z.; Peng, J.; Xu, L.; Liu, P. Development and Application of Surface-Enhanced Raman Scattering (SERS). *Nano-Mater.* **2024**, *14*, 1417. [CrossRef]
33. Jensen, L.; Aikens, C.M.; Schatz, G.C. Electronic Structure Methods for Studying Surface-Enhanced Raman Scattering. *Chem. Soc. Rev.* **2008**, *37*, 1061. [CrossRef]
34. Cong, S.; Liu, X.; Jiang, Y.; Zhang, W.; Zhao, Z. Surface Enhanced Raman Scattering Revealed by Interfacial Charge-Transfer Transitions. *Innovation* **2020**, *1*, 100051. [CrossRef]
35. Gu, Y.; Li, Y.; Qiu, H.; Yang, Y.; Wu, Q.; Fan, X.; Ding, Y.; Yi, L.; Ge, K.; Shen, Y. Recent Progress on Noble-Free Substrates for Surface-Enhanced Raman Spectroscopy Analysis. *Coord. Chem. Rev.* **2023**, *497*, 215425. [CrossRef]
36. Wen, B.-Y.; Chen, Q.-Q.; Radjenovic, P.M.; Dong, J.-C.; Tian, Z.-Q.; Li, J.-F. In Situ Surface-Enhanced Raman Spectroscopy Characterization of Electrocatalysis with Different Nanostructures. *Annu. Rev. Phys. Chem.* **2021**, *72*, 331–351. [CrossRef]
37. Yi, J.; You, E.-M.; Hu, R.; Wu, D.-Y.; Liu, G.-K.; Yang, Z.-L.; Zhang, H.; Gu, Y.; Wang, Y.-H.; Wang, X.; et al. Sur-face-Enhanced Raman Spectroscopy: A Half-Century Historical Perspective. *Chem. Soc. Rev.* **2025**, *54*, 1453–1551. [CrossRef]
38. Goel, R.; Chakraborty, S.; Awasthi, V.; Bhardwaj, V.; Dubey, S.K. Exploring the Various Aspects of Surface Enhanced Raman Spectroscopy (SERS) with Focus on the Recent Progress: SERS-Active Substrate, SERS-Instrumentation, SERS-Application. *Sensors Actuators A Phys.* **2024**, *376*, 115555. [CrossRef]
39. Van Duyne, R.P.; Haushalter, J.P. Surface-Enhanced Raman Spectroscopy of Adsorbates on Semiconductor Electrode Sur-faces: Tris(Bipyridine)Ruthenium(II) Adsorbed on Silver-Modified n-Gallium Arsenide(100). *J. Phys. Chem.* **1983**, *87*, 2999–3003. [CrossRef]
40. Fleischmann, M.; Tian, Z.Q.; Li, L.J. Raman Spectroscopy of Adsorbates on Thin Film Electrodes Deposited on Silver Sub-strates. *J. Electroanal. Chem. Interfacial Electrochem.* **1987**, *217*, 397–410. [CrossRef]
41. Leung, L.W.H.; Weaver, M.J. Extending Surface-Enhanced Raman Spectroscopy to Transition-Metal Surfaces: Carbon Monoxide Adsorption and Electrooxidation on Platinum- and Palladium-Coated Gold Electrodes. *J. Am. Chem. Soc.* **1987**, *109*, 5113–5119. [CrossRef]
42. Langer, J.; De Aberasturi, D.J.; Aizpurua, J.; Alvarez-Puebla, R.A.; Auguié, B.; Baumberg, J.J.; Bazan, G.C.; Bell, S.E.J.; Boisen, A.; Brolo, A.G.; et al. Present and Future of Surface-Enhanced Raman Scattering. *Acs Nano* **2020**, *14*, 28–117. [CrossRef] [PubMed]
43. Zhang, H.; Duan, S.; Radjenovic, P.M.; Tian, Z.-Q.; Li, J.-F. Core–Shell Nanostructure-Enhanced Raman Spectroscopy for Surface Catalysis. *Acc. Chem. Res.* **2020**, *53*, 729–739. [CrossRef] [PubMed]
44. Haryanto, A.; Lee, C.W. Shell Isolated Nanoparticle Enhanced Raman Spectroscopy for Mechanistic Investigation of Electrochemical Reactions. *Nano Converg.* **2022**, *9*, 9. [CrossRef]
45. Huh, J.-H.; Lee, J.; Lee, S. Comparative Study of Plasmonic Resonances between the Roundest and Randomly Faceted Au Nanoparticles-on-Mirror Cavities. *Acs Photonics* **2018**, *5*, 413–421. [CrossRef]
46. Feng, R.; Fu, S.; Liu, H.; Wang, Y.; Liu, S.; Wang, K.; Chen, B.; Zhang, X.; Hu, L.; Chen, Q.; et al. Single-Atom Site SERS Chip for Rapid, Ultrasensitive, and Reproducible Direct-Monitoring of RNA Binding. *Adv. Healthc. Mater.* **2024**, *13*, 2301146. [CrossRef]
47. Chen, B.; Meng, S.; Liu, D.; Deng, Q.; Wang, C. In Situ SERS Monitoring of Schiff Base Reactions via Nanoparticles on a Mirror Platform. *Catalysts* **2024**, *14*, 803. [CrossRef]
48. Mahapatra, S.; Li, L.; Schultz, J.F.; Jiang, N. Tip-Enhanced Raman Spectroscopy: Chemical Analysis with Nanoscale to Angstrom Scale Resolution. *J. Chem. Physics* **2020**, *153*, 010902. [CrossRef]
49. Wessel, J. Surface-Enhanced Optical Microscopy. *J. Opt. Soc. Am. B* **1985**, *2*, 1538. [CrossRef]
50. Stöckle, R.M.; Suh, Y.D.; Deckert, V.; Zenobi, R. Nanoscale Chemical Analysis by Tip-Enhanced Raman Spectroscopy. *Chem. Phys. Lett.* **2000**, *318*, 131–136. [CrossRef]
51. Hayazawa, N.; Inouye, Y.; Sekkat, Z.; Kawata, S. Metallized Tip Amplification of Near-Field Raman Scattering. *Opt. Commun.* **2000**, *183*, 333–336. [CrossRef]

52. Zhang, Z.; Sheng, S.; Wang, R.; Sun, M. Tip-Enhanced Raman Spectroscopy. *Anal. Chem.* **2016**, *88*, 9328–9346. [CrossRef] [PubMed]
53. Niu, T.; Yuan, Y.; Yao, J.; Lu, F.; Gu, R. Structure of Water at Ionic Liquid/Ag Interface Probed by Surface Enhanced Raman Spectroscopy. *Sci. China Chem.* **2011**, *54*, 200–204. [CrossRef]
54. Chen, G.-Y.; Sun, Y.-B.; Shi, P.-C.; Liu, T.; Li, Z.-H.; Luo, S.-H.; Wang, X.-C.; Cao, X.-Y.; Ren, B.; Liu, G.-K.; et al. Revealing Unconventional Host–Guest Complexation at Nanostructured Interface by Surface-Enhanced Raman Spectroscopy. *Light. Sci. Appl.* **2021**, *10*, 85. [CrossRef]
55. Ma, W.; Wang, Y.; Wang, R.; Fan, X.; Ma, S.; Tang, Y.; Ai, Z.; Yao, Y.; Zhang, L.; Gao, T. Azo-Enhanced Raman Scattering Probing Proton Transfer between Water and Nanoscale Zero-Valent Iron. *J. Am. Chem. Soc.* **2024**, *146*, 32785–32794. [CrossRef]
56. Zhang, J.; Peng, M.; Lian, E.; Xia, L.; Asimakopoulos, A.G.; Luo, S.; Wang, L. Identification of Poly(Ethylene Terephthalate) Nanoplastics in Commercially Bottled Drinking Water Using Surface-Enhanced Raman Spectroscopy. *Environ. Sci. Technol.* **2023**, *57*, 8365–8372. [CrossRef] [PubMed]
57. Liu, C.; Lei, F.; Gong, M.; Zhou, X.; Zhao, X.; Li, Z.; Zhang, C.; Man, B.; Yu, J. In Situ Raman Monitoring of Trace Antibiotics in Different Harsh Water Environments. *Energy Environ. Mater.* **2024**, *7*, e12517. [CrossRef]
58. Dou, X.; Zhao, L.; Li, X.; Qin, L.; Han, S.; Kang, S.-Z. Ag Nanoparticles Decorated Mesh-like MoS2 Hierarchical Nanostructure Fabricated on Ti Foil: A Highly Sensitive SERS Substrate for Detection of Trace Malachite Green in Flowing Water. *Appl. Surf. Sci.* **2020**, *509*, 145331. [CrossRef]
59. Hu, R.; Zhang, K.; Wang, W.; Wei, L.; Lai, Y. Quantitative and Sensitive Analysis of Polystyrene Nanoplastics down to 50 nm by Surface-Enhanced Raman Spectroscopy in Water. *J. Hazard. Mater.* **2022**, *429*, 128388. [CrossRef]
60. Ruan, X.; Xie, L.; Liu, J.; Ge, Q.; Liu, Y.; Li, K.; You, W.; Huang, T.; Zhang, L. Rapid Detection of Nanoplastics down to 20 nm in Water by Surface-Enhanced Raman Spectroscopy. *J. Hazard. Mater.* **2024**, *462*, 132702. [CrossRef]
61. Carreón, R.V.; Cortázar-Martínez, O.; Rodríguez-Hernández, A.G.; De La Rosa, L.E.S.; Gervacio-Arciniega, J.J.; Krishnan, S.K. Ionic Liquid-Assisted Thermal Evaporation of Bimetallic Ag–Au Nanoparticle Films as a Highly Reproducible SERS Substrate for Sensitive Nanoplastic Detection in Complex Environments. *Anal. Chem.* **2024**, *96*, 5790–5797. [CrossRef]
62. Carreón, R.V.; Rodríguez-Hernández, A.G.; De La Rosa, L.E.S.; Gervacio-Arciniega, J.J.; Krishnan, S.K. Mechanically Flexible, Large-Area Fabrication of Three-Dimensional Dendritic Au Films for Reproducible Surface-Enhanced Raman Scat-tering Detection of Nanoplastics. *Acs Sens.* **2025**, *10*, 1747–1755. [CrossRef]
63. Xing, F.; Duan, W.; Tang, J.; Zhou, Y.; Guo, Z.; Zhang, H.; Xiong, J.; Fan, M. Superhydrophobic Surface-Enhanced Raman Spectroscopy (SERS) Substrates for Sensitive Detection of Trace Nanoplastics in Water. *Anal. Chem.* **2025**, *97*, 2293–2299. [CrossRef]
64. Li, G.; Yang, Z.; Pei, Z.; Li, Y.; Yang, R.; Liang, Y.; Zhang, Q.; Jiang, G. Single-Particle Analysis of Micro/Nanoplastics by SEM-Raman Technique. *Talanta* **2022**, *249*, 123701. [CrossRef] [PubMed]
65. Li, Y.; Fu, J.; Peng, L.; Sun, X.; Wang, G.; Wang, Y.; Chen, L. A Sustainable Emulsion for Separation and Raman Identification of Microplastics and Nanoplastics. *Chem. Eng. J.* **2023**, *469*, 143992. [CrossRef]
66. Shao, Q.; Zhang, X.; Liang, P.; Chen, Q.; Qi, X.; Zou, M. Fabrication of Magnetic Au/Fe3O4/MIL-101(Cr) (AF-MIL) as Sensitive Surface-Enhanced Raman Spectroscopy (SERS) Platform for Trace Detection of Antibiotics Residue. *Appl. Surf. Sci.* **2022**, *596*, 153550. [CrossRef]
67. Feng, Y.; Dai, J.; Wang, C.; Zhou, H.; Li, J.; Ni, G.; Zhang, M.; Huang, Y. Ag Nanoparticle/Au@Ag Nanorod Sandwich Structures for SERS-Based Detection of Perfluoroalkyl Substances. *Acs Appl. Nano Mater.* **2023**, *6*, 13974–13983. [CrossRef]
68. Kukralova, K.; Miliutina, E.; Guselnikova, O.; Burtsev, V.; Hrbek, T.; Svorcik, V.; Lyutakov, O. Dual-Mode Electrochemical and SERS Detection of PFAS Using Functional Porous Substrate. *Chemosphere* **2024**, *364*, 143149. [CrossRef]
69. Lada, Z.G.; Mathioudakis, G.N.; Beobide, A.S.; Andrikopoulos, K.S.; Voyiatzis, G.A. Generic Method for the Detection of Short & Long Chain PFAS Extended to the Lowest Concentration Levels of SERS Capability. *Chemosphere* **2024**, *363*, 142916. [CrossRef] [PubMed]
70. Mohajer, M.A.; Basuri, P.; Evdokimov, A.; David, G.; Zindel, D.; Miliordos, E.; Signorell, R. Spontaneous formation of urea from carbon dioxide and ammonia in aqueous droplets. *Science* **2025**, *388*, 1426–1430. [CrossRef]
71. Zhang, X.; Huang, Q.; Liu, Y.-X.; Yin, J.; Pang, S.-F.; Liu, P.; Zhang, Y.-H.; Ge, M. Microdroplet Surface Drives and Accel-erates Proton-Controlled, Size-Dependent Nitrate Photolysis. *J. Am. Chem. Soc.* **2025**, *147*, 19595–19601. [CrossRef]
72. Li, K.; Ge, Q.; Liu, Y.; Wang, L.; Gong, K.; Liu, J.; Xie, L.; Wang, W.; Ruan, X.; Zhang, L. Highly Efficient Photocatalytic H2 O2 Production in Microdroplets: Accelerated Charge Separation and Transfer at Interfaces. *Energy Environ. Sci.* **2023**, *16*, 1135–1145. [CrossRef]
73. Wang, W.; Liu, Y.; Wang, T.; Ge, Q.; Li, K.; Liu, J.; You, W.; Wang, L.; Xie, L.; Fu, H.; et al. Significantly Accelerated Pho-tosensitized Formation of Atmospheric Sulfate at the Air–Water Interface of Microdroplets. *J. Am. Chem. Soc.* **2024**, *146*, 6580–6590. [CrossRef] [PubMed]
74. Wan, L.; Ding, X.-L.; Liu, A.-X.; Cui, H.; Zhong, J.-R.; Dai, Y.-M. Biodegradable MAM-Based Amphiphilic Block Copolymers: Toward Efficient and Eco-Friendly Kinetic Inhibitors for Methane Hydrate Formation. *Chem. Eng. J.* **2024**, *500*, 157347. [CrossRef]

75. Li, K.; You, W.; Wang, W.; Gong, K.; Liu, Y.; Wang, L.; Ge, Q.; Ruan, X.; Ao, J.; Ji, M.; et al. Significantly Accelerated Pho-tochemical Perfluorooctanoic Acid Decomposition at the Air–Water Interface of Microdroplets. *Environ. Sci. Technol.* **2023**, *57*, 21448–21458. [CrossRef]
76. Hao, G.; Shu-Xi, D.; Cheng-Feng, S.; Chao, W.; Ya-Bin, H.; Zu-Liang, D. In Situ Raman Spectroscopy of Langmuir Mono-layers at Air-Water Interface. *Acta Phys.-Chim. Sin.* **2006**, *22*, 1061–1064. [CrossRef]
77. Arunagiri, V.; Prasannan, A.; Udomsin, J.; Lai, J.-Y.; Wang, C.-F.; Hong, P.-D.; Tsai, H.C. Facile Fabrication of Eco-Friendly Polycaprolactone (PCL)/Poly-D, L-Lactic Acid (PDLLA) Modified Melamine Sorbent for Oil-Spill Cleaning and Water/Oil (W/O) Emulsion Separation. *Sep. Purif. Technol.* **2021**, *259*, 118081. [CrossRef]
78. Qiang, F.; Hu, L.-L.; Gong, L.-X.; Zhao, L.; Li, S.-N.; Tang, L.-C. Facile Synthesis of Super-Hydrophobic, Electrically Con-ductive and Mechanically Flexible Functionalized Graphene Nanoribbon/Polyurethane Sponge for Efficient Oil/Water Sep-aration at Static and Dynamic States. *Chem. Eng. J.* **2018**, *334*, 2154–2166. [CrossRef]
79. Fischer, B.; Lambertz, A.; Nuys, M.; Beyer, W.; Duan, W.; Bittkau, K.; Ding, K.; Rau, U. Insights into the Si–H Bonding Configuration at the Amorphous/Crystalline Silicon Interface of Silicon Heterojunction Solar Cells by Raman and FTIR Spectroscopy. *Adv. Mater.* **2023**, *35*, 2306351. [CrossRef]
80. Luo, Y.; Liu, Y.; Feng, H.; Liang, H.; Shen, J.; Diao, Y.; Liu, Y.; Zeng, X.; Yu, Z.; Sun, R.; et al. In Situ Raman Spectroscopy Monitoring of Interface Aging in Aluminum-Filled Polydimethylsiloxane Composites. *Nano Mater. Sci.* **2025**, S2589965125000558. [CrossRef]
81. Lee, C.; Jeong, B.G.; Yun, S.J.; Lee, Y.H.; Lee, S.M.; Jeong, M.S. Unveiling Defect-Related Raman Mode of Monolayer WS2 via Tip-Enhanced Resonance Raman Scattering. *Acs Nano* **2018**, *12*, 9982–9990. [CrossRef]
82. Shao, J.; Chen, F.; Su, W.; Zeng, Y.; Lu, H.-W. Multimodal Nanoscopic Study of Atomic Diffusion and Related Localized Optoelectronic Response of WS2 /MoS2 Lateral Heterojunctions. *Acs Appl. Mater. Interfaces* **2021**, *13*, 20361–20370. [CrossRef]
83. Garg, S.; Fix, J.P.; Krayev, A.V.; Flanery, C.; Colgrove, M.; Sulkanen, A.R.; Wang, M.; Liu, G.-Y.; Borys, N.J.; Kung, P. Na-noscale Raman Characterization of a 2D Semiconductor Lateral Heterostructure Interface. *Acs Nano* **2022**, *16*, 340–350. [CrossRef]
84. Rahaman, M.; Marino, E.; Joly, A.G.; Stevens, C.E.; Song, S.; Alfieri, A.; Jiang, Z.; O'Callahan, B.T.; Rosen, D.J.; Jo, K.; et al. Tunable Localized Charge Transfer Excitons in Nanoplatelet–2D Chalcogenide van Der Waals Heterostructures. *Acs Nano* **2024**, *18*, 15185–15193. [CrossRef]
85. Milekhin, I.A.; Rahaman, M.; Anikin, K.V.; Rodyakina, E.E.; Duda, T.A.; Saidzhonov, B.M.; Vasiliev, R.B.; Dzhagan, V.M.; Milekhin, A.G.; Latyshev, A.V.; et al. Resonant Tip-Enhanced Raman Scattering by CdSe Nanocrystals on Plasmonic Sub-strates. *Nanoscale Adv.* **2020**, *2*, 5441–5449. [CrossRef]
86. Meng, G.; Chan, J.C.K.; Rousseau, D.; Li-Chan, E.C.Y. Study of Protein−Lipid Interactions at the Bovine Serum Albumin/Oil Interface by Raman Microspectroscopy. *J. Agric. Food Chem.* **2005**, *53*, 845–852. [CrossRef] [PubMed]
87. Niu, F.; Niu, D.; Zhang, H.; Chang, C.; Gu, L.; Su, Y.; Yang, Y. Ovalbumin/Gum Arabic-Stabilized Emulsion: Rheology, Emulsion Characteristics, and Raman Spectroscopic Study. *Food Hydrocoll.* **2016**, *52*, 607–614. [CrossRef]
88. Han, Z.; Xu, S.; Sun, J.; Yue, X.; Wu, Z.; Shao, J.-H. Effects of Fatty Acid Saturation Degree on Salt-Soluble Pork Protein Conformation and Interfacial Adsorption Characteristics at the Oil/Water Interface. *Food Hydrocoll.* **2021**, *113*, 106472. [CrossRef]
89. Wang, S.; Liu, X.; Zhao, G.; Li, Y.; Yang, L.; Zhu, L.; Liu, H. Protease-Induced Soy Protein Isolate (SPI) Characteristics and Structure Evolution on the Oil–Water Interface of Emulsion. *J. Food Eng.* **2022**, *317*, 110849. [CrossRef]
90. Wang, Y.; Zhu, Y.; Gupta, P.; Singamaneni, S.; Lee, B.; Jun, Y.-S. The Roles of Oil–Water Interfaces in Forming Ultrasmall CaSO4 Nanoparticles. *Acs Appl. Mater. Interfaces* **2024**, *16*, 29390–29401. [CrossRef] [PubMed]
91. He, S.; Jin, X.; Wang, D.; Hao, D.; Li, Y.; Zhu, Z.; Tian, Y.; Jiang, L. Interfacial Water-Dictated Oil Adhesion Based on Ion Modulation. *J. Am. Chem. Soc.* **2023**, *145*, 24145–24152. [CrossRef]
92. Hu, Y.; Sun, Y.; Xia, Q.; Du, L.; He, J.; Xu, J.; Zhou, C.; Pan, D. Hydrophobic Interaction at the O/W Interface: Impacts on the Interfacial Stability, Encapsulation and Bioaccessibility of Polyphenols. *Food Hydrocoll.* **2023**, *140*, 108622. [CrossRef]
93. Tomobe, K.; Yamamoto, E.; Kojić, D.; Sato, Y.; Yasui, M.; Yasuoka, K. Origin of the Blueshift of Water Molecules at Interfaces of Hydrophilic Cyclic Compounds. *Sci. Adv.* **2017**, *3*, e1701400. [CrossRef]
94. Taylor, J.N.; Bando, K.; Tsukagoshi, S.; Tanaka, L.; Fujita, K.; Fujita, S. Microscopic Water Dispersion and Hydrogen-Bonding Structures in Margarine Spreads with Raman Hyperspectral Imaging and Machine Learning. *Food Chem.* **2025**, *465*, 142035. [CrossRef] [PubMed]
95. Zhang, J.; Zhang, W.; Hao, J.; Li, X.; Xu, D.; Cao, Y. In Vitro Digestion of Solid-in-Oil-in-Water Emulsions for Delivery of CaCO3. *Food Hydrocoll.* **2022**, *129*, 107605. [CrossRef]
96. Guo, D.; Ou, W.; Ning, F.; Fang, B.; Liu, Z.; Fang, X.; Lu, W.; Zhang, L.; Din, S.U.; He, Z. The Effects of Hydrate Formation and Dissociation on the Water-Oil Interface: Insight into the Stability of an Emulsion. *Fuel* **2020**, *266*, 116980. [CrossRef]
97. Phan-Quang, G.C.; Lee, H.K.; Ling, X.Y. Isolating Reactions at the Picoliter Scale: Parallel Control of Reaction Kinetics at the Liquid–Liquid Interface. *Angew. Chem. Int. Ed.* **2016**, *55*, 8304–8308. [CrossRef]

98. Xiong, H.; Lee, J.K.; Zare, R.N.; Min, W. Strong Electric Field Observed at the Interface of Aqueous Microdroplets. *J. Phys. Chem. Lett.* **2020**, *11*, 7423–7428. [CrossRef]
99. Argyri, S.-M.; Stark, A.; Eriksson, V.; Evenäs, L.; Martinelli, A.; Bordes, R. Crystallization at the Hexadecane/Water Interface Observed under Acoustic Levitation. *J. Environ. Sci.* **2025**, *158*, 197–206. [CrossRef]
100. Lin, X.-M.; Sun, Y.-L.; Chen, Y.-X.; Li, S.-X.; Li, J.-F. Insights into Electrocatalysis through in Situ Electrochemical Sur-face-Enhanced Raman Spectroscopy. *EScience* **2024**, 100352. [CrossRef]
101. Liu, S.; D'Amario, L.; Jiang, S.; Dau, H. Selected Applications of Operando Raman Spectroscopy in Electrocatalysis Research. *Curr. Opin. Electrochem.* **2022**, *35*, 101042. [CrossRef]
102. Fleischmann, M.; Hendra, P.J.; McQuillan, A.J. Raman Spectra from Electrode Surfaces. *J. Chem. Soc., Chem. Commun.* **1973**, *80*. [CrossRef]
103. Wu, D.-Y.; Li, J.-F.; Ren, B.; Tian, Z.-Q. Electrochemical Surface-Enhanced Raman Spectroscopy of Nanostructures. *Chem. Soc. Rev.* **2008**, *37*, 1025. [CrossRef]
104. Shi, L.; LaCour, R.A.; Qian, N.; Heindel, J.P.; Lang, X.; Zhao, R.; Head-Gordon, T.; Min, W. Water Structure and Electric Fields at the Interface of Oil Droplets. *Nature* **2025**, *640*, 87–93. [CrossRef] [PubMed]
105. Wen, J.; Tang, S.; Wu, X.; Xu, L.; Xie, Y.; Yin, Y.; Song, F. Unraveling the Mechanism of Hydrogen Evolution Reactions in Alkaline Media: Recent Advances in in Situ Raman Spectroscopy. *Chem. Commun.* **2025**, *61*, 8778–8789. [CrossRef] [PubMed]
106. Li, C.-Y.; Le, J.-B.; Wang, Y.-H.; Chen, S.; Yang, Z.-L.; Li, J.-F.; Cheng, J.; Tian, Z.-Q. In Situ Probing Electrified Interfacial Water Structures at Atomically Flat Surfaces. *Nat. Mater.* **2019**, *18*, 697–701. [CrossRef] [PubMed]
107. Wang, Y.-H.; Zheng, S.; Yang, W.-M.; Zhou, R.-Y.; He, Q.-F.; Radjenovic, P.; Dong, J.-C.; Li, S.; Zheng, J.; Yang, Z.-L.; et al. In Situ Raman Spectroscopy Reveals the Structure and Dissociation of Interfacial Water. *Nature* **2021**, *600*, 81–85. [CrossRef]
108. You, X.; Zhang, D.; Zhang, X.-G.; Li, X.; Tian, J.-H.; Wang, Y.-H.; Li, J.-F. Exploring the Cation Regulation Mechanism for Interfacial Water Involved in the Hydrogen Evolution Reaction by In Situ Raman Spectroscopy. *Nano-Micro Lett.* **2024**, *16*, 53. [CrossRef]
109. Shen, L.; Lu, B.; Li, Y.; Liu, J.; Huang-fu, Z.; Peng, H.; Ye, J.; Qu, X.; Zhang, J.; Li, G.; et al. Interfacial Structure of Water as a New Descriptor of the Hydrogen Evolution Reaction. *Angew. Chem. Int. Ed.* **2020**, *59*, 22397–22402. [CrossRef]
110. Zhao, K.; Chang, X.; Su, H.; Nie, Y.; Lu, Q.; Xu, B. Enhancing Hydrogen Oxidation and Evolution Kinetics by Tuning the Interfacial Hydrogen-Bonding Environment on Functionalized Platinum Surfaces. *Angew. Chem. Int. Ed.* **2022**, *61*, e202207197. [CrossRef]
111. Zhou, S.; Cao, W.; Shang, L.; Zhao, Y.; Xiong, X.; Sun, J.; Zhang, T.; Yuan, J. Facilitating Alkaline Hydrogen Evolution Ki-netics via Interfacial Modulation of Hydrogen-Bond Networks by Porous Amine Cages. *Nat. Commun.* **2025**, *16*, 1849. [CrossRef]
112. Xiang, L.; Leng, D.; Zhang, X.; Li, H.; Wang, H.; Pi, C.; Wu, S.; Huang, L.; Li, Y.; Huo, K.; et al. PtO Nanoclusters on Ul-tra-Thin 2D Mo2C Enhance Hydrated Cation Interaction for Superior Alkaline Hydrogen Evolution Reaction. *J. Colloid. Interface Sci.* **2025**, *688*, 22–31. [CrossRef]
113. Cao, D.; Gao, P.; Shen, Y.; Qiao, L.; Ma, M.; Guo, X.; Cheng, D. Fabricating Lattice-Confined Pt Single Atoms with High Electron-Deficient State for Alkali Hydrogen Evolution Under Industrial-Current Density. *Adv. Mater.* **2025**, *37*, 2414138. [CrossRef]
114. Xu, G.-Y.; Yue, M.-F.; Qian, Z.-X.; Du, Z.-Y.; Xie, X.-Q.; Chen, W.-P.; Zhang, Y.-J.; Li, J.-F. Metal-Support Interactions Alter the Active Species on IrO x for Electrocatalytic Water Oxidation. *J. Mater. Chem. A* **2023**, *11*, 15204–15210. [CrossRef]
115. Dong, J.; Qian, Z.; Xu, P.; Yue, M.-F.; Zhou, R.-Y.; Wang, Y.; Nan, Z.-A.; Huang, S.; Dong, Q.; Li, J.-F.; et al. In Situ Raman Spectroscopy Reveals the Structure Evolution and Lattice Oxygen Reaction Pathway Induced by the Crystalline–Amorphous Heterojunction for Water Oxidation. *Chem. Sci.* **2022**, *13*, 5639–5649. [CrossRef]
116. Cho, K.H.; Park, S.; Seo, H.; Choi, S.; Lee, M.Y.; Ko, C.; Nam, K.T. Capturing Manganese Oxide Intermediates in Electro-chemical Water Oxidation at Neutral pH by In Situ Raman Spectroscopy. *Angew. Chem. Int. Ed.* **2021**, *60*, 4673–4681. [CrossRef]
117. Hu, Y.; Hu, C.; Du, A.; Xiao, T.; Yu, L.; Yang, C.; Xie, W. Interfacial Evolution on Co-Based Oxygen Evolution Reaction Electrocatalysts Probed by Using In Situ Surface-Enhanced Raman Spectroscopy. *Anal. Chem.* **2022**, *95*, 1703–1709. [CrossRef] [PubMed]
118. Ram, R.; Xia, L.; Benzidi, H.; Guha, A.; Golovanova, V.; Manjón, A.G.; Rauret, D.L.; Berman, P.S.; Dimi-tropoulos, M.; Mundet, B.; et al. Water-Hydroxide Trapping in Cobalt Tungstate for Proton Exchange Membrane Water Electrolysis. *Science* **2024**, *384*, 1373–1380. [CrossRef] [PubMed]
119. Zhou, Y.; Zhao, L.; Xu, G.; Wang, N.; Chen, X.; Wang, Z.; Kong, D.; Yang, X.; Meng, C. H* Site-Blocking Alleviated Through Collaborative Copper Alloying for Large-Current Hydrogen Production. *Adv. Energy Mater.* **2025**, 2501852. [CrossRef]
120. Scheu, R.; Chen, Y.; De Aguiar, H.B.; Rankin, B.M.; Ben-Amotz, D.; Roke, S. Specific Ion Effects in Amphiphile Hydration and Interface Stabilization. *J. Am. Chem. Soc.* **2014**, *136*, 2040–2047. [CrossRef] [PubMed]
121. Judd, K.D.; De Oliveira, D.M.; Urbina, A.S.; Ben-Amotz, D. Influence of H+, OH− and Salts on Hydrophobic Self-Assembly. *Chem. Sci.* **2024**, *15*, 6378–6384. [CrossRef]

122. Wentworth, C.M.; Myers, R.L.; Cremer, P.S.; Zarzar, L.D. Investigating Oil Solubilization into Nonionic Micelles by Raman Multivariate Curve Resolution: Special Collection: Aggregation-Induced Processes and Functions. *Aggregate* **2023**, *4*, e385. [CrossRef]
123. Davis, J.G.; Gierszal, K.P.; Wang, P.; Ben-Amotz, D. Water Structural Transformation at Molecular Hydrophobic Interfaces. *Nature* **2012**, *491*, 582–585. [CrossRef] [PubMed]
124. Hossain, I.M.; Pooja, N.; Kondeti, S.S.C.; Yamamoto, T.; Mazumder, N.; Noothalapati, H. Direct Estimation of Amylose and Amylopectin in Single Starch Granules by Machine Learning Assisted Raman Spectroscopy. *Carbohydr. Polym.* **2025**, *366*, 123929. [CrossRef] [PubMed]
125. Ahmad, W.; Zareef, M.; Chen, M.; Xu, Y.; Wang, J.; Chen, Q. Surface-Enhanced Raman Scattering Detection of Antibiotics. *TrAC Trends Anal. Chem.* **2025**, *191*, 118352. [CrossRef]

Disclaimer/Publisher's Note: The statements, opinions and data contained in all publications are solely those of the individual author(s) and contributor(s) and not of MDPI and/or the editor(s). MDPI and/or the editor(s) disclaim responsibility for any injury to people or property resulting from any ideas, methods, instructions or products referred to in the content.